Materials & Design 223 (2022) 111117

Contents lists available at ScienceDirect

Materials & Design

journal homepage: www.elsevier.com/locate/matdes

Increasing the interlayer strength of 3D printed concrete with tooth-like interface: An experimental and theoretical investigation

Lewei He [a,b], Hua Li [b,*], Wai Tuck Chow [b], Biqing Zeng [a], Ye Qian [c,*]

[a] School of Software, South China Normal University, Foshan 528225, People's Republic of China
[b] School of Mechanical and Aerospace Engineering, Nanyang Technological University, 50 Nanyang Avenue, Singapore 639798, Republic of Singapore
[c] Department of Civil Engineering, The University of Hong Kong, Pokfulam Road, Hong Kong, People's Republic of China

HIGHLIGHTS

- Improvements of interlayer tensile strength by 291% and shear strength by 89% are achieved by interface tooth angle of 45°.
- Interlayer strength is theoretically modeled by tooth angle, void ratio, and the ratio between adhesion and cohesion.
- Validation is conducted with a relative error of about 5% and the strengths decently included in the prediction envelope.
- Within 5-min interval, voids decrease the interlayer strength notably. Otherwise, adhesion degradation is more impactful.

GRAPHICAL ABSTRACT

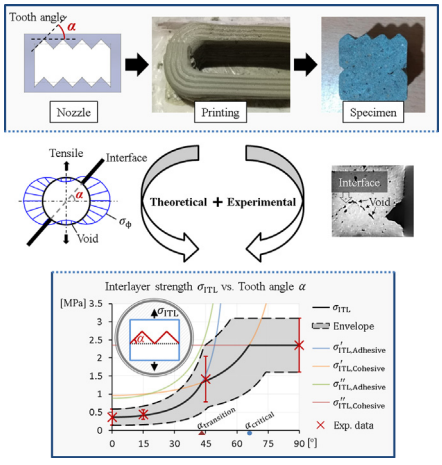

ARTICLE INFO

Article history:
Received 30 April 2022
Revised 23 August 2022
Accepted 4 September 2022
Available online 6 September 2022

Keywords:
3D concrete printing
Interlayer strength
Failure mode
Interfacial geometry
Interfacial void ratio
Interfacial adhesion

ABSTRACT

In 3D concrete printing, layer interface and interlayer notch are generated by the layer-by-layer process. Therefore, the 3D printed concrete is anisotropic with the interlayer strength lower than the strengths measured in the other two directions. In order to adequately address this issue, tooth-like layer interface is adopted in the present study for higher interlayer strength. It is found that the tooth-like interface with tooth angle of 45° increases the interlayer tensile and shear strengths by 294% and 89% respectively, and shifts the failure mode from pure adhesive failure to a mixture of adhesive and cohesive failures. Moreover, a theoretical model is developed for the relationship between the interlayer strength and interfacial tooth angle, and then validated by the experimental data with a relative error of about 5%. By this model, further design and optimization of the interfacial geometry would be possible, for higher interlayer strength subject to different parameters and conditions of 3D concrete printing.

1. Introduction

3D concrete printing is gaining popularity among institutes and companies throughout the world due to its potential in the building and construction industry [1–3]. Compared with traditional

* Corresponding authors.
E-mail addresses: lihua@ntu.edu.sg (H. Li), yjqian@hku.hk (Y. Qian).

https://doi.org/10.1016/j.matdes.2022.111117
0264-1275/

construction techniques, 3D concrete printing provides larger design freedom with shortened program duration, reduced human labor and minimized material waste [4,5]. However, the layer interface of 3D printed concrete is inherently weaker than the layer matrix due to the layer-by-layer process of 3D concrete printing [6,7], and thus anisotropy exists in the printed concrete with the lowest tensile strength perpendicular to the layer interface [8–10]. It was reported that the interlayer strength dropped to about 40 % of the matrix strength [11], and degraded to an even lower percentage with dry underlay surface [6], large nozzle stand-off distance [5], long interlayer printing interval [12–14], etc. Therefore, strong anisotropy and low interlayer strength that hinder the application of 3D concrete printing demand a prompt and effective solution [11].

The degradation of interfacial adhesion results from a higher content of hydration byproducts (e.g. $Ca(OH)_2$ and ettringite) at the layer interface than that in the layer matrix [15–17]. Moreover, numerous voids at the interface also play a pivotal role in the interlayer failure due to stress concentration and smaller bonding area [18–21]. Tay *et al.* [12] related the interfacial void ratio to the layer interval and rheological properties of material, and explained that the underlying concrete built up yield stress and stiffness with longer layer interval, leading to worse interlayer contact, more interfacial voids, and thus lower interlayer strength [22–24]. Although techniques were proposed to reduce the interlayer voids [25,26], some entrained voids might still remain at the interface and thus strongly affect the interlayer strength due to stress concentration.

A compendious review on interfacial lack of fusion was conducted by Kruger *et al.* [27], and they attributed the lack of fusion to four main factors, namely surface moisture, air entrapment, thixotropy and surface roughness. It was reported that a lubrication layer formed between the hose and the included material during the extrusion, since the moisture oozed from the concrete under extrusion pressure and moved towards the hose lining [28]. Meanwhile, the fine aggregates of concrete migrated from the lining to the centre of the hose due to shear gradient [29]. As a consequence, the lubrication layer exhibited higher water/cement ratio and led to higher colloidal porosity at the layer interface when the overlay concrete was deposited [30]. Worse still, macro voids might be produced at the interface due to water migration between two layers [27]. It was reasoned that the underlay lost moisture due to evaporation and became drier than the freshly deposited overlay [14], and thus the underlay absorbed water from the overlay while drove the air in the underlay to the layer interface [27]. Although the pumping pressure reduced the total void volume and broke large voids into small voids [30], voids with larger equivalent diameters concentrated at the interface with elongated and flattened morphology along the printing direction [31], making the interface more vulnerable under tensile, compressive and shear loadings [32,33]. Moreover, it was clearly observed by Kruger *et al.* [31] that higher printing speed and longer interlayer interval resulted in higher porosity at the interface, and the voids increased above the interface and decreased below the interface probably due to the water migration from overlay to underlay.

For higher interlayer strength, the underlying concrete is usually roughened by water jetting or sand blasting before the repair paste is applied to the concrete [34–36] in the field of concrete repair and rehabilitation [37,38]. However, these techniques for hardened concrete are not applicable to 3D concrete printing where the underlying concrete is still not fully hardened. Zareiyan *et al.* [20] studied the effect of interface interlocking by multi-layer casting and found that the interlayer strength is related to the size of interlocking. Wang *et al.* [39] improved the bonding between prefabricated 3D printed concrete parts with different adhesives and interlocking geometries, and found that epoxy-based adhesive and V-type interlocking performed the best. He *et al.* investigated the effect of nozzle shape and produced tooth-like geometries at the layer interface during printing with an increase of the interlayer strength by 55 % [40,41]. Interfacial adhesives were also applied to the layer interface and an increase of interlayer strength by up to 167 % was observed [42,43]. Interestingly, the effect of interfacial tooth angle between PDMS rubber and acrylate was recently studied and tremendous improvement of the bonding was made by Ding *et al.* [44]. However, the interlayer strength was still lower than the matrix strength with the above techniques, and the issue of anisotropy was not addressed yet [26,45].

In terms of anisotropic modeling of 3D printed concrete, some important achievements were made. Xiao *et al.* [46] used concrete damaged plasticity model for the concrete matrix and cohesive elements with traction-separation law for the interfaces between filaments in the same layer and those between layers. They found that the number of interface (or the filament dimensions) influenced the ultimate strengths of a specimen, and confirmed that the compressive strength achieved the highest along the filament direction since shear at the interface was the minimum. Van den Heever *et al.* [32] took another approach, such that they regarded the printed concrete as a continuum and adopted the anisotropic Rankine-Hill (RH) model based on both tested and assumed parameters. It was observed that this technique accurately captured the elastic, peak and ultimate responses of 3D printed concrete to tensile and flexure loadings, with only limited deviation on the post-peak behavior. This continuum-based technique could also model the anisotropic matrix strength of 3D printed concrete produced by the microstructural voids elliptically shaped along the printing direction [32].

In the present work, tooth-like layer interfaces are fabricated elaborately in order to increase both the interlayer tensile and shear strengths. Based on the experimental results, this study also aims to develop a novel theoretical model, which relates the interlayer strength to the topological modified interface and further expresses the strength analytically with various interface characteristics, in order to take an important step toward the interfacial geometry optimization of 3D printed concrete.

2. Materials and methodology

2.1. Materials

As shown in Table 1 for the composition and Fig. 1 for the sieve size, the material by Tay *et al.* [12] is adopted in the present study due to its verified pumpability and buildability. The dry components namely Ordinary Portland Cement (Grade 42.5), fly ash (Class F), silica fume (undensified), and river sand are mixed by a Hobart mixer at 59 rpm for 5 mins. Water is subsequently added and mixed with the dry components at 59 rpm for 1 min, and then at 198 rpm for another 7 mins [12].

2.2. Nozzle design

In order to increase the interlayer strength of 3D printed concrete yet without any extra material cost that is incurred, the idea of tooth-like interfacial geometry is taken from the pioneer work by B. Zareiyan & B. Khoshnevis [20]. As shown in Fig. 2, the impact of stress concentration on the layer interface varies with different inclination angles α, due to different moduli of circumferential stress σ_ϕ with reference tensile stress σ_{ref} subject to different polar coordinates ϕ. For instance, a horizontal interface ($\alpha = 0$) passes through the center of stress concentration and experiences very high level of stress, while an inclined interface deviates from the center of stress concentration and thus is much less affected.

Table 1
Material composition design by weight [12].

Cement to binder ratio	Fly ash to binder ratio	Silica fume to binder ratio	Sand to binder ratio	Water to binder ratio
0.7	0.2	0.1	1.2	0.46

Note: Binder comprises cement, fly ash and silica fume.

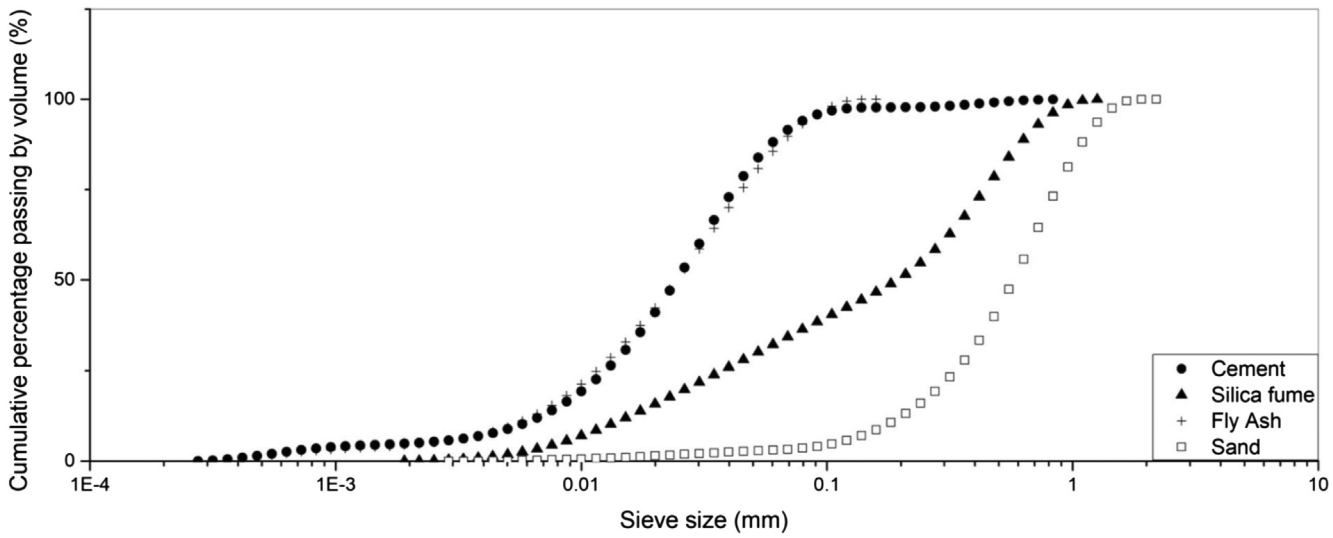

Fig. 1. Cumulative percentage passing by volume for all particles by Ref. [12]. Figure reprinted from the journal Virtual and Physical Prototyping, 14 (2019) 104–113, Y.W.D. Tay, G.H.A. Ting, Y. Qian, B. Panda, L. He, M.J. Tan, Time gap effect on bond strength of 3D-printed concrete [12], with permission from Taylor & Francis ltd, www.tandfonline.com.

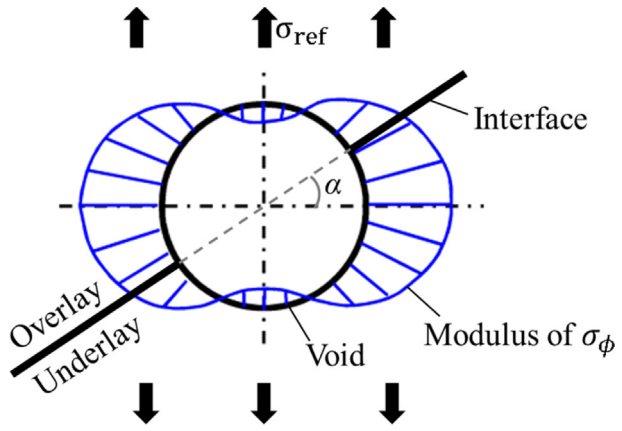

Fig. 2. Modulus of the circumferential stress σ_ϕ produced by a circular void at the layer interface with reference tensile stress σ_{ref}.

Therefore, in order to generate inclined layer interface and improve the interlayer bonding, a nozzle with tooth-like geometry is proposed and prototyped, as shown in Fig. 3, in contrast to the traditional circular and rectangular nozzles [47–49]. A nozzle connector is also designed, as shown in Fig. 4, such that the concrete is extruded from the nozzle and then laid on the previous layer with little deformation [50,51], and thus the tooth-like geometry of the nozzle becomes that of the layer interface. Tooth angles $\alpha = 15^\circ$ and $\alpha = 45^\circ$ are selected in the present study, while a rectangular nozzle with the same outlet area is also adopted and denoted by $\alpha = 0^\circ$ for comparison.

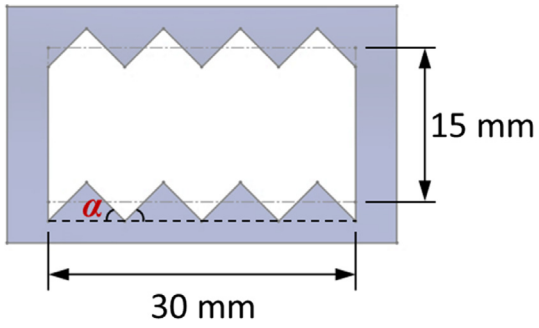

Fig. 3. Layout of the tooth-like nozzle.

2.3. Printing and sample preparation

8 layers of concrete are printed by a Mitsubishi gantry and a Mai cavity pump with a printing speed of 80 mm/s and layer interval of about 10 s. The printed concrete is then covered by a plastic sheet and maintained in laboratory environment at 25 ℃ for 28 days. As shown in Figs. 5, 13 packages of raw specimen are collected, with a specimen thickness of 30 mm and 4 specimens in each package from the layer 1 to the layer 8 in order to establish a more universal design principle of the tooth-like interface. The flat and tooth-like layer interfaces are well generated with interfacial voids and a pair of interlayer notches, as shown in Fig. 6(a). In order to eliminate the impact of the notch on the interlayer strength [52–54], the specimens in 5 packages undergo post processing such that the notch is removed from the tip by a diamond cutter, as shown in Fig. 6(b).

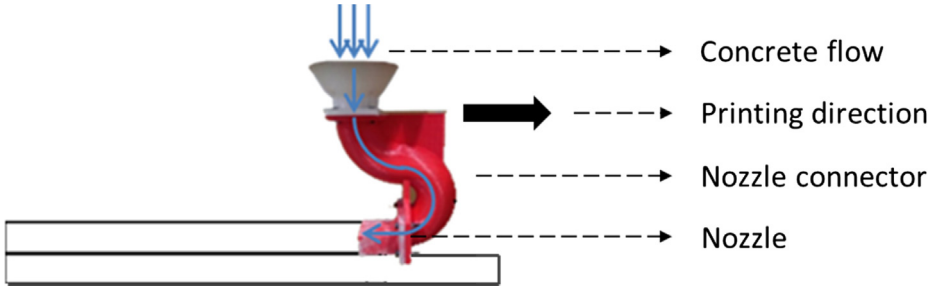

Fig. 4. Illustration of the printing process.

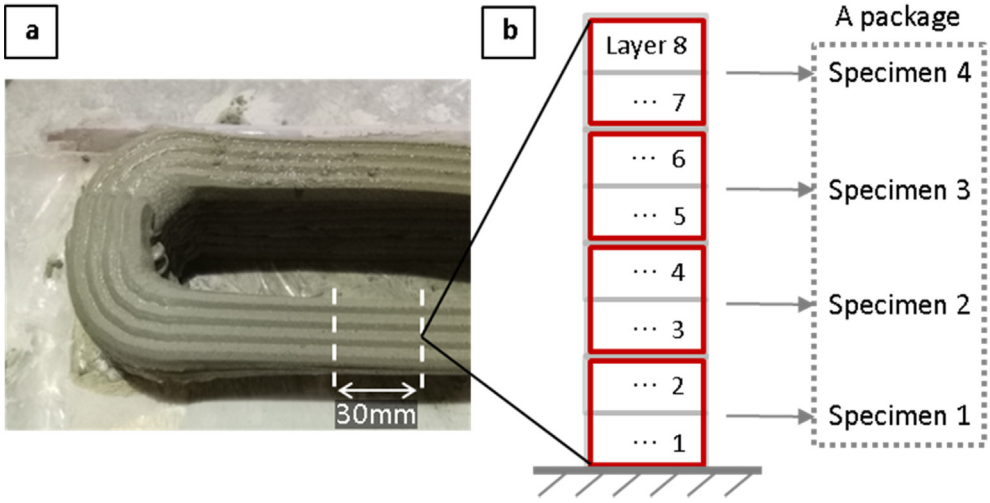

Fig. 5. (a) The 3D printed concrete and (b) collection of the specimens.

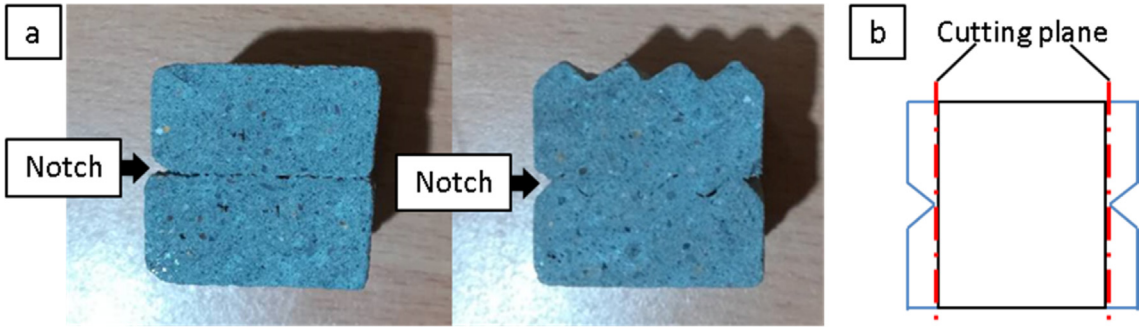

Fig. 6. Illustrations of (a) raw specimens and (b) removal of the interlayer notch.

2.4. Tensile test

As shown in Table 2, tensile tests are labeled by the interfacial geometries of the specimen and whether the notch is removed, such that the suffix (R) stands for the scenario with raw specimen and reserved interlayer notch, $\alpha = 0^{\circ}$ for the flat interface, $\alpha = 15^{\circ}$ for the interface with tooth angle 15°, $\alpha = 45^{\circ}$ for the interface with tooth angle 45°, and $\alpha = 90^{\circ}$ for the matrix test with vertically aligned interface.

In order to measure the interlayer tensile strength σ_{ITL} and matrix tensile strength σ_{Matrix}, specimens are glued to the fixture by epoxy resin in two different directions, as shown in Fig. 7. The tensile tests are conducted at a constant loading rate of 0.5 mm/min with each test scenario based on the 4 specimens in a package.

Table 2
Experimental design for the tensile test.

	Interlayer test ($\alpha = 0^{\circ}$)	Interlayer test ($\alpha = 15^{\circ}$)	Interlayer test ($\alpha = 45^{\circ}$)	Matrix test ($\alpha = 90^{\circ}$)
Raw	$\sigma_{ITL,\,0^{\circ}}$ (R)		$\sigma_{ITL,\,45^{\circ}}$ (R)	σ_{Matrix}
Notch removed	$\sigma_{ITL,\,0^{\circ}}$	$\sigma_{ITL,\,15^{\circ}}$	$\sigma_{ITL,\,45^{\circ}}$	

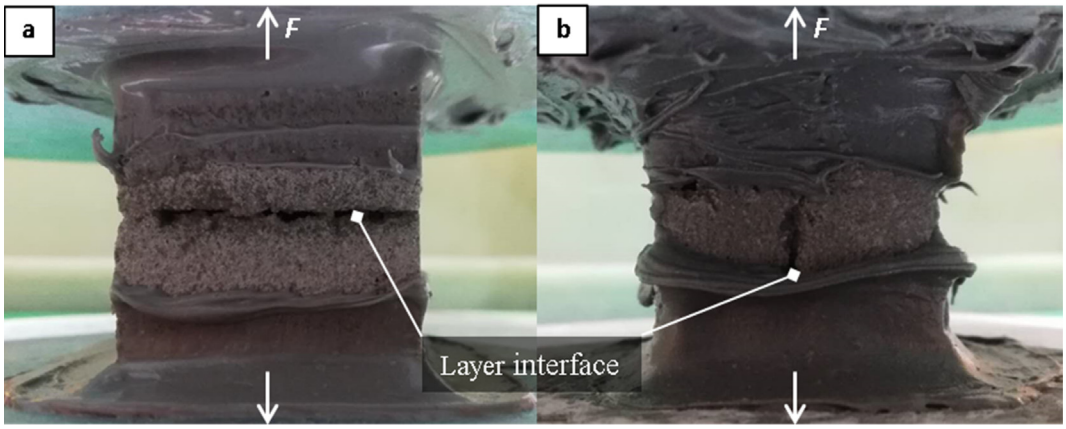

Fig. 7. Tensile test configurations for (a) interlayer strength σ_{ITL} and (b) matrix strength σ_{Matrix}.

The maximum tensile load F and the cross-sectional area A perpendicular to the load are recorded, and thus σ_{ITL} and σ_{Matrix} are calculated by.

$$\sigma_{ITL},\ \sigma_{Matrix} = \frac{F}{A} \tag{1}$$

2.5. Shear test

As shown in Table 3, shear tests are labeled by the interfacial geometries and whether the notch is removed, such that the suffix (R) stands for the scenario with raw specimen and preserved interlayer notch, $\alpha = 0^{\circ}$ for the flat interface, $\alpha = 45^{\circ}$ for the interface with tooth angle 45°, and $\alpha = 90^{\circ}$ for the matrix test with vertically aligned interface. Meanwhile, the interlayer shear test is conducted in two directions, such that the roman numeral I represents the first interlayer shear direction along the printing, and II represents the second interlayer shear direction perpendicular to the printing.

As shown in Fig. 8, the interlayer shear strengths $\tau_{ITL\,I}$, $\tau_{ITL\,II}$, and matrix shear strength τ_{Matrix} are measured at a constant loading rate of 0.5 mm/min and each test scenario is based on the 4 specimens in a package. The specimens are held by an aluminum frame with horizontal distances a = 80 mm and b = 320 mm between the cylinder supports, as shown in Fig. 9, and finite adjustment is allowed between the specimen and the frame in order to prevent a three-point bending scenario. If the maximum force applied to the loading beam is F, the maximum shear load S on the specimen is calculated by [55].

$$S = [(b-a)/(b+a)]F \tag{2}$$

Then the interlayer shear strength τ_{ITL} and matrix shear strength τ_{Matrix} are calculated by [56].

$$\tau_{ITL},\ \tau_{Matrix} = \frac{S}{A} \tag{3}$$

where A is the cross-sectional area of the specimen on the shear plane.

3. Experimental results

3.1. Results of the tensile test

In this section, experimental results of the tensile test are presented. As shown in Fig. 10, the failure modes are photographed for the specimens in the tensile test. It is not surprising that the matrix tensile test yields cohesive failure, which is regarded as the ideal mode and usually correlated to the highest strength [57–59]. Although pure cohesive failure is not yielded by the interlayer tensile tests, a mixed mode of cohesive and adhesive failures is produced by the specimens with both removed interlayer notch and interfacial tooth angle $\alpha = 45^{\circ}$. Meanwhile, other groups yield pure adhesive failure that implies improper interlayer bonding [20,60]. It is noteworthy that adhesive failure happens if the interlayer notch exists or the tooth angle α is small (0° or 15°), indicating that large tooth angle α together with removal of the interlayer notch benefits the interlayer bonding at tensile load.

The interlayer tensile strength σ_{ITL} and matrix tensile strength σ_{Matrix} produced by the raw specimens (R) with interlayer notch are shown in Fig. 11. It is seen that $\sigma_{ITL} = 0.37$ MPa is produced by the specimens with flat interface ($\alpha = 0^{\circ}$), and $\sigma_{ITL} = 0.78$ MPa by the specimens with interfacial tooth angle $\alpha = 45^{\circ}$. Both of the interlayer strengths σ_{ITL} are lower than the matrix strength $\sigma_{Matrix} = 2.35$ MPa.

The interlayer tensile strength σ_{ITL} produced by the specimens with removed interlayer notch is shown in Fig. 12. It is found that removal of the interlayer notch increases σ_{ITL} by about 81 % for the samples with tooth angle $\alpha = 45^{\circ}$, while it does not change the interlayer strength for the samples with flat interface (0.37 MPa with notch and 0.36 MPa without notch). This phenomenon is

Table 3
Experimental design for the shear test.

	Interlayer test ($\alpha = 0^{\circ}$)	Interlayer test ($\alpha = 45^{\circ}$)	Matrix test ($\alpha = 90^{\circ}$)
I (Raw)	$\tau_{ITL\,I,0^{\circ}}$ (R)	$\tau_{ITL\,I,45^{\circ}}$ (R)	τ_{Matrix}
I (Notch removed)	$\tau_{ITL\,I,0^{\circ}}$	$\tau_{ITL\,I,45^{\circ}}$	
II (Raw)	$\tau_{ITL\,II,0^{\circ}}$ (R)	$\tau_{ITL\,II,45^{\circ}}$ (R)	
II (Notch removed)	$\tau_{ITL\,II,0^{\circ}}$	$\tau_{ITL\,II,45^{\circ}}$	

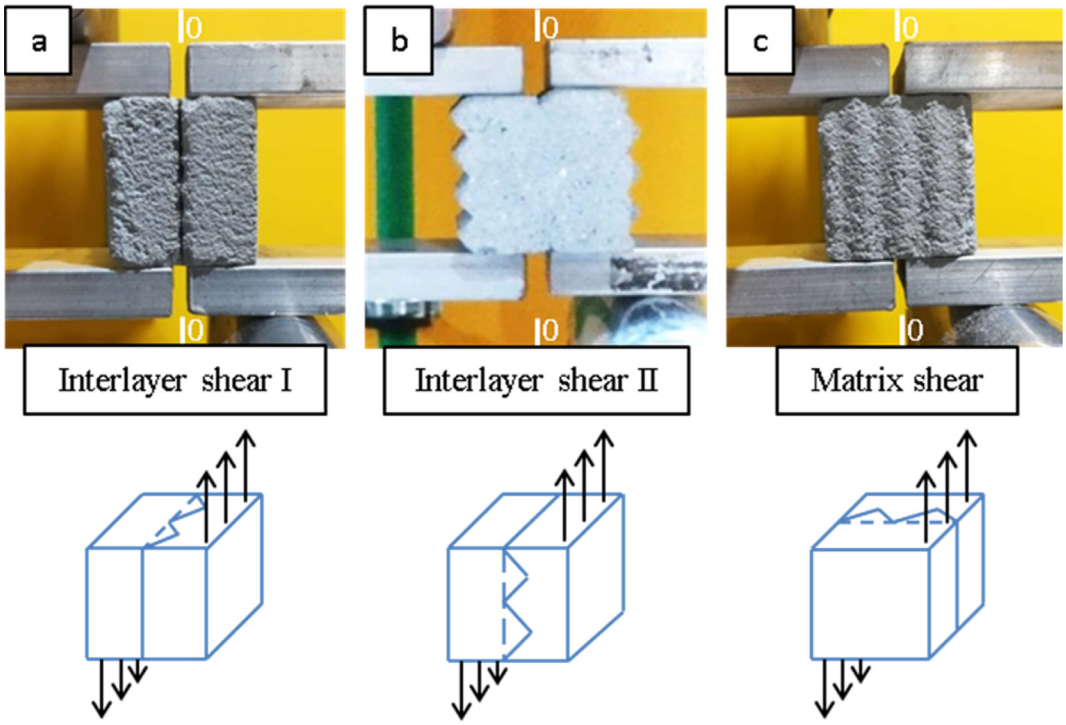

Fig. 8. Three directions of the shear test (zeros denote the shear plane).

explained that the interlayer failure at flat interface is mainly initiated by the voids if they are abundant at the interface, while the impact of the interfacial voids becomes lower at tooth-like interface and thus the interlayer notch also plays a part in the interlayer failure.

In order to eliminate the impact of the interlayer notch and have a clearer insight into the tooth angle effect, the present study is more focused on the specimens with removed interlayer notch. It is noticed that the interlayer strength σ_{ITL} increases with the tooth angle α at a nonlinear rate in the specimens without interlayer notch, such that the effect of tooth angle α is negligible when α is small, while α becomes much more influential when it is larger than 15°. For instance, the interlayer strength with a flat interface is $\sigma_{ITL,\,0^\circ} = 0.36(\text{MPa})$, and tooth angle $\alpha = 15^\circ$ marginally increases the strength to $\sigma_{ITL,\,15^\circ} = 0.43(\text{MPa})$ (about 119 % of $\sigma_{ITL,\,0^\circ}$), while tooth angle $\alpha = 45^\circ$ significantly increases the strength to $\sigma_{ITL,\,45^\circ} = 1.42(\text{MPa})$ (about 394 % of $\sigma_{ITL,\,0^\circ}$).

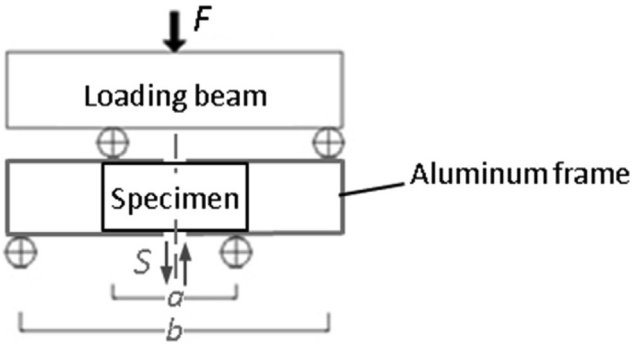

Fig. 9. Setup of the shear test.

3.2. Results of the shear test

As shown in Fig. 13, the failure modes are photographed for the specimens in the shear test. It is noticed that cohesive failure is also generated by the matrix shear test, same to the mode by the matrix tensile test. According to the analysis by Gideon P.A.G. van Zijl [61], diagonal failure occurs in shear test when the volume of polyethylene fibre is less than 2 %, due to an equivalent biaxial tension and compression principal stress state in the diagonal direction. Therefore, cracks are generated with the increased diagonal tensile strain, and finally a fracture surface with an inclination angle of about 15° is observed in the matrix shear test due to the constraint of the fixture. By the interlayer shear tests however, a mixture of cohesive and adhesive failures is yielded by the specimens with interfacial tooth angle $\alpha = 45^\circ$, while pure adhesive failure is yielded by the specimens with the flat interface ($\alpha = 0^\circ$). It is thus concluded that the failure mode in the shear test is not as much affected by the interlayer notch as that in the tensile test, probably because the notch is the most harmful with perpendicular tensile stress, while the interlayer shear stress is decomposed into a pair of tensile and compressive stresses 45 degrees from the notch.

The interlayer shear strengths $\tau_{ITL\,I}(R)$, $\tau_{ITL\,II}(R)$, and matrix strength τ_{Matrix} produced by the raw specimens with interlayer notch are calculated by Eqs. (2)–(3), and shown in Fig. 14. It is also seen that the interlayer strengths $\tau_{ITL}(R)$ with interfacial tooth angle $\alpha = 45^\circ$ are higher than those with the flat interface $\alpha = 0^\circ$ in both shear directions I & II, although still much lower than the matrix shear strength τ_{Matrix}. In order to focus on the tooth angle effect without the impact of the interlayer notch, specimens with removed notch are also studied but in shear direction I only, since quite similar trends are observed in the two shear directions.

As shown in Fig. 15, removal of the interlayer notch does not increase $\tau_{ITL\,I}$ significantly with the flat interface ($\alpha = 0^\circ$), while it increases $\tau_{ITL\,I}$ with interfacial tooth angle $\alpha = 45^\circ$, probably

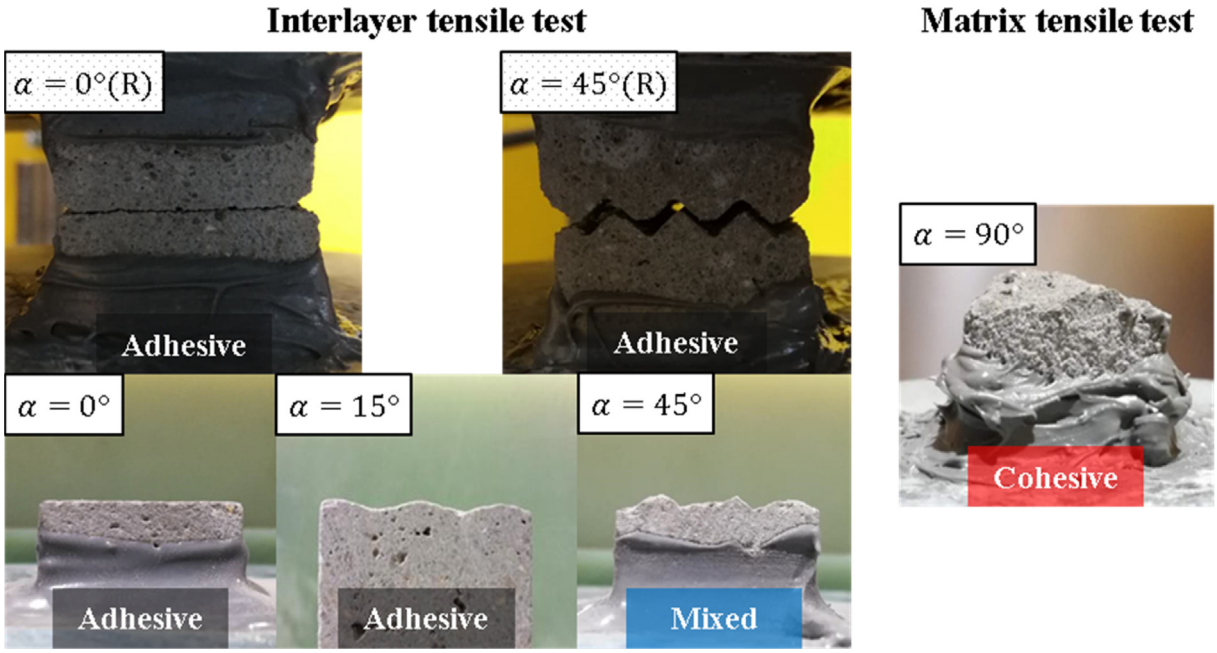

Fig. 10. Failure modes in the tensile test.

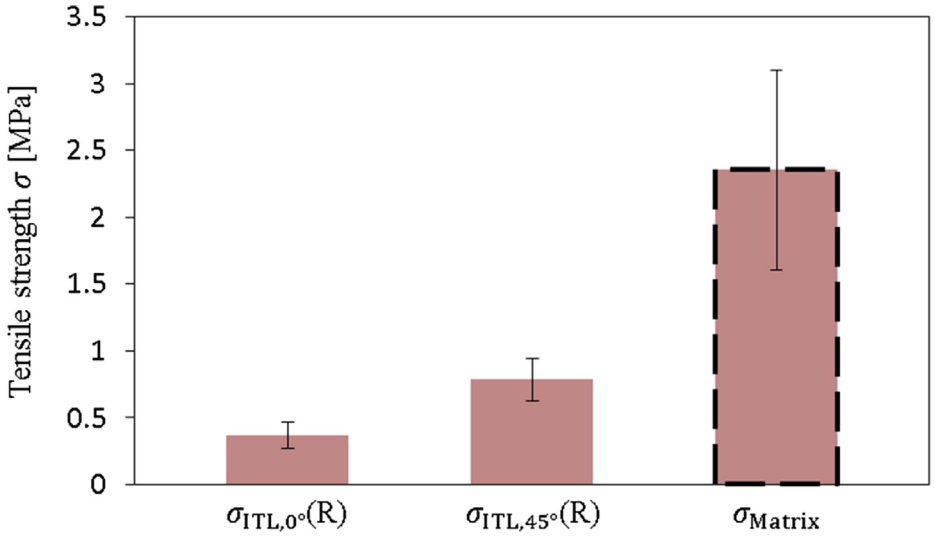

Fig. 11. Tensile strengths σ of the raw specimens (R) with the interlayer notch.

because the impact of interfacial voids is reduced at the tooth-like interface and thus the interlayer notch starts to take effect as well. Moreover, it is noticed that the tooth angle α increases the interlayer shear strength $\tau_{\mathrm{ITL\,I}}$ also at a nonlinear rate. For instance, the interlayer shear strength with a flat interface is $\tau_{\mathrm{ITL\,I},\,0^\circ} = 2.22(\mathrm{MPa})$, and it increases with the tooth angle α at a lower rate to $\tau_{\mathrm{ITL\,I},\,45^\circ} = 4.19(\mathrm{MPa})$, then at a higher rate to $\tau_{\mathrm{Matrix}} = 7.41(\mathrm{MPa})$. These experimental data produced by the specimens with removed interlayer notch are used to validate the theoretical model in Section 4.2.

3.3. Characterization of the interfacial voids between layers

As shown in Figs. 16-18, CT-scan, optical-microscopic and scanning electron microscopic (SEM) images from low to high resolution are provided in order to have a close observation of the interfacial voids. It is found that the interfacial voids are flattened vertically and elongated along the interface, similar to the elliptic topology that was illustrated in Ref. [30]. However, an ellipse is determined by the semi-axes a and b with the inclination angle α, and an analytical expression of its stress field requires both affine transformation and complex-variable functions [62,63]. Therefore, the interfacial voids are simplified tentatively into circular shape for the theoretical modeling in Section 4.1. Interfacial void ratio r is defined by the sum of void lengths $\sum l_{\mathrm{void}}$ over the length of interface $l_{\mathrm{interface}}$ in a specimen cross section,

$$r = \frac{\sum l_{\mathrm{void}}}{l_{\mathrm{interface}}} \tag{4}$$

and $r = 0.59$ with its standard deviation $\mathrm{Std}(r) = 0.13$ is calculated based on equally-spaced four CT-scan images with flat interface and another four with tooth-like interface.

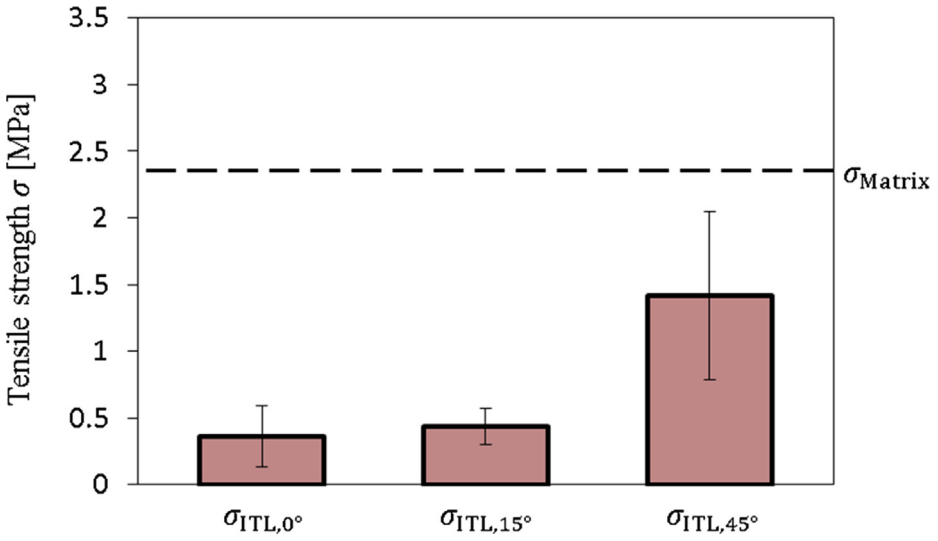

Fig. 12. Tensile strengths σ of the specimens with removed interlayer notch.

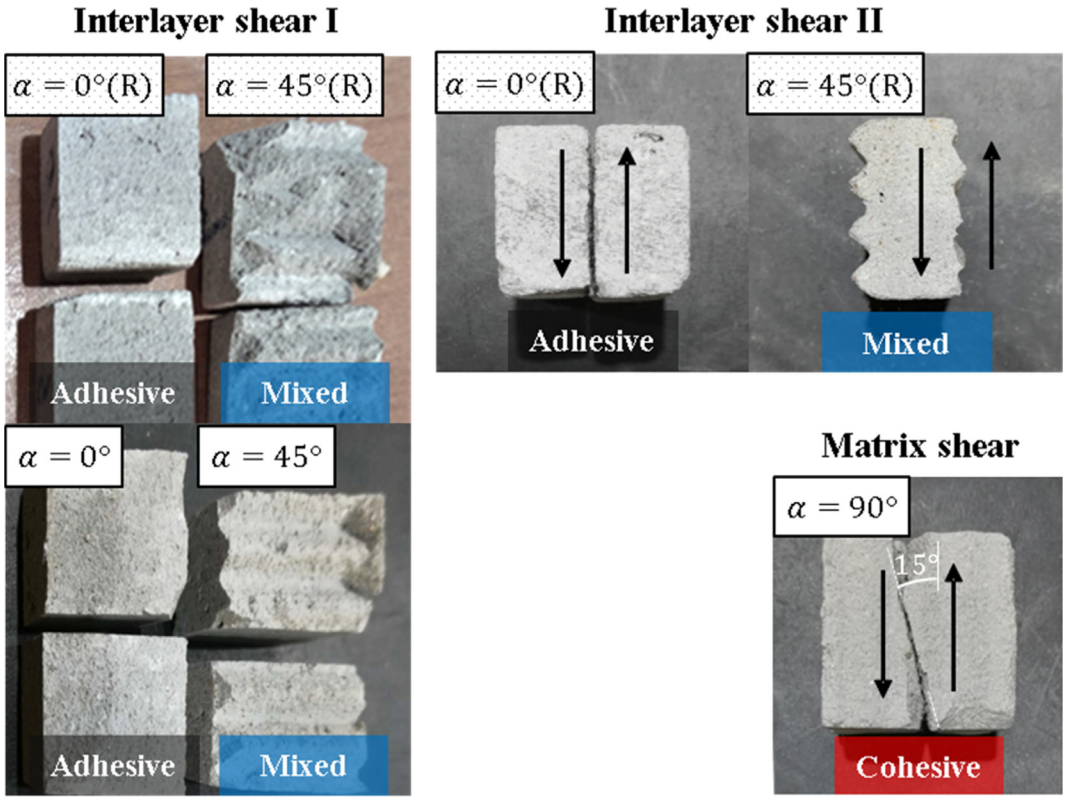

Fig. 13. Failure modes in the shear test.

4. Modeling and discussions

4.1. Theoretical model

In this study, tooth angle α determines the interfacial area between two layers. However, the effect of interfacial area is not explanatory enough for the increase of interlayer strength σ_{ITL} with larger tooth angle α, since $\sigma_{ITL,45^\circ}$ is about 4 times of $\sigma_{ITL,0^\circ}$ from the experimental data while the interfacial area only increases by about 40 %. In order to understand the relationship between interlayer tensile strength σ_{ITL} and interface parameters, namely the tooth angle α and void ratio r, interfacial voids are simplified into uniformly distributed circular holes and a 2-D theoretical model is developed based on the stress-concentration phenomenon and the following assumptions:

1) Due to stress concentration, circumferential stress σ_ϕ of a representative void is calculated by [64,65],

$$\sigma_\phi = \sigma_{ref} \times (1 + 2\cos 2\phi) \quad (5)$$

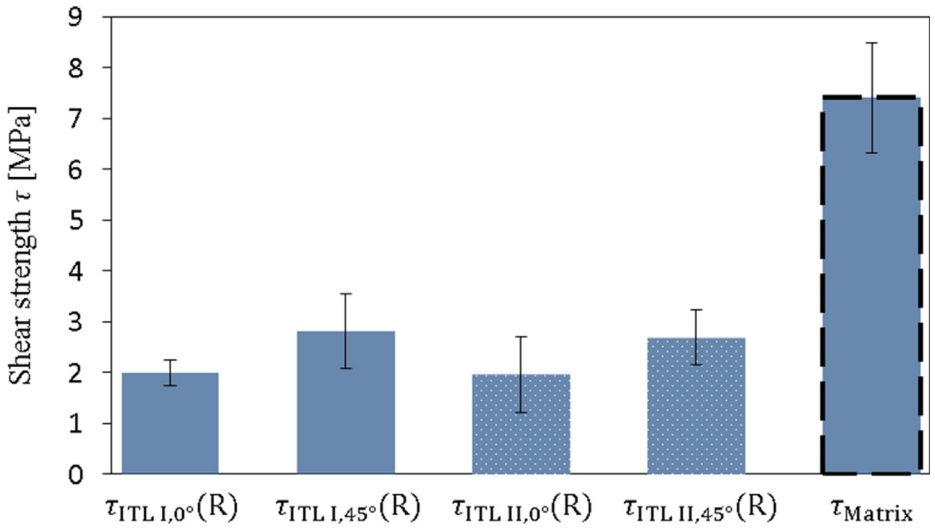

Fig. 14. Shear strengths τ of the raw specimens (R) with interlayer notch in the directions I & II.

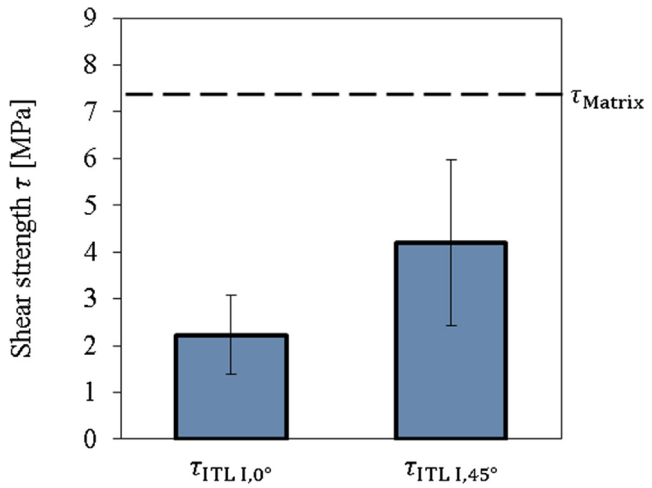

Fig. 15. Shear strengths τ of the specimens with removed interlayer notch in the direction I.

where ϕ is the polar coordinate of a representative void, and σ_{ref} the reference uniaxial stress when failure is initiated. σ_ϕ reaches the maximum at the horizontal apex ($\phi = 0$).

2) Adhesive failure is initiated if the circumferential stress σ_ϕ at the interface $\sigma_\phi|_{\phi=\alpha}$ is equal to the adhesion σ_{adhesion} of interface,

$$\sigma_\phi|_{\phi=\alpha} = \sigma_{\text{adhesion}} \tag{6}$$

3) Cohesive failure is initiated if the circumferential stress σ_ϕ at the horizontal apex $\sigma_\phi|_{\phi=0}$ is equal to the cohesion σ_{cohesion} of layer matrix,

$$\sigma_\phi|_{\phi=0} = \sigma_{\text{cohesion}} \tag{7}$$

4) The reference stress σ_{ref} in Eq. (5) is estimated by the external load F over the specimen thickness T times l,

$$\sigma_{\text{ref}} = \frac{F}{T \times l} \tag{8}$$

where l is the length of the shortest "path" over the specimen excluding the voids, such that the shortest "path" is either horizontal or along the interface depending on the tooth angle α and void ratio r, as shown in Fig. 19. Therefore, the "path" length l is calculated by,

$$l = \begin{cases} \frac{L}{\cos\alpha} \times (1-r), \alpha \le \alpha_{\text{critical}} \\ L, \alpha > \alpha_{\text{critical}} \end{cases} \tag{9}$$

where L is the width of the specimen and the critical angle α_{critical} indicates the tooth angle α when $L \times (\cos\alpha)^{-1} \times (1-r) = L$, which is thus calculated by,

$$\alpha_{\text{critical}} = \cos^{-1}(1-r) \tag{10}$$

Since the interlayer strength σ_{ITL} is calculated by the maximum tensile load F over the specimen width L and thickness T,

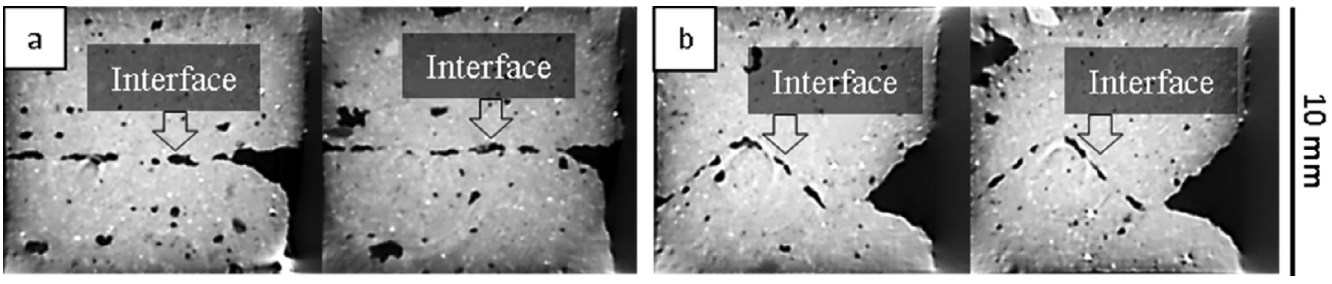

Fig. 16. CT-scan images of (a) the flat ($\alpha = 0^\circ$) and (b) tooth-like ($\alpha = 45^\circ$) interfaces.

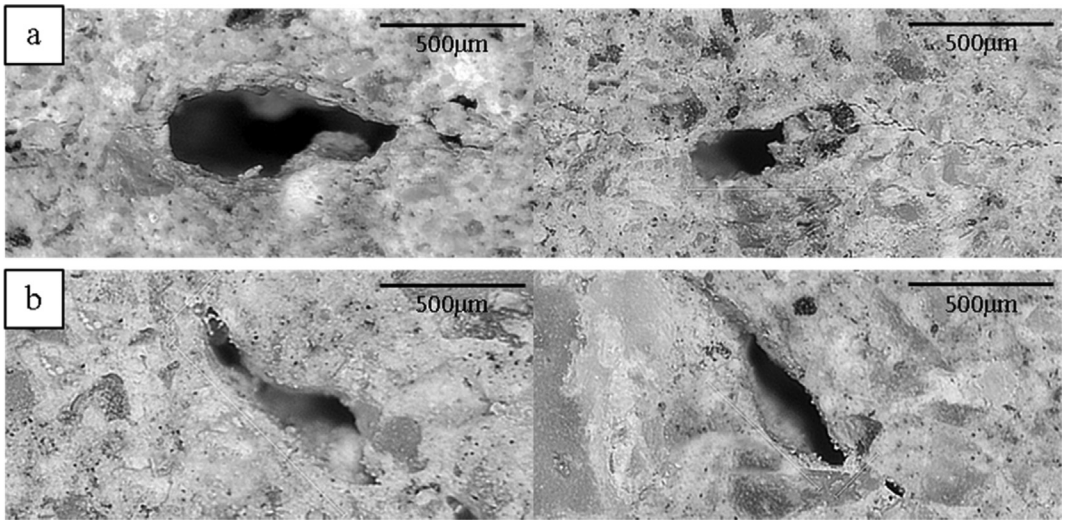

Fig. 17. Optical-microscopic images of the voids at (a) the flat ($\alpha = 0^{\circ}$) and (b) tooth-like ($\alpha = 45^{\circ}$) interfaces.

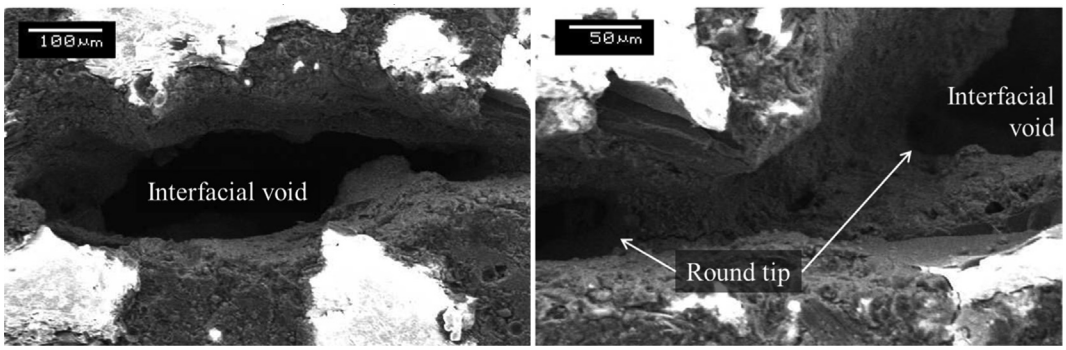

Fig. 18. Scanning electron microscopic (SEM) images of the interfacial voids with round tips.

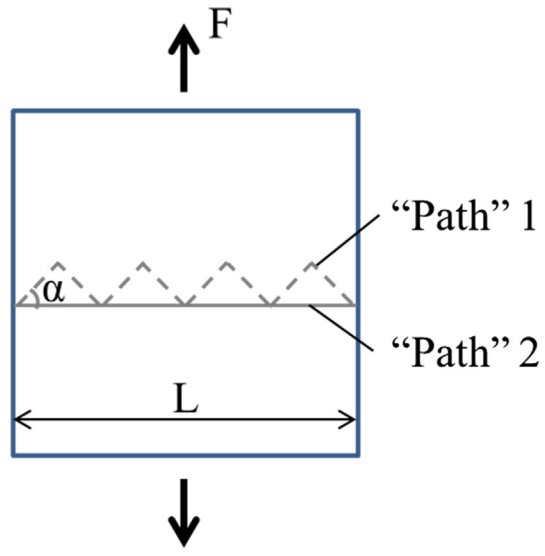

Fig. 19. Illustration of the two fictitious paths over the cross section.

$$\sigma_{ITL} = \frac{F}{L \times T} \tag{11}$$

it is then expressed by σ_{ref} multiplied by a coefficient l/L with substitution of Eq. (8) into Eq. (11),

$$\sigma_{ITL} = \sigma_{ref} \times \frac{l}{L} \tag{12}$$

Therefore, interlayer tensile strengths σ_{ITL} due to the adhesive and cohesive failures are calculated respectively by solving the reference stress σ_{ref} with Eqs. (5), (6) and (7), and then substituting σ_{ref} into Eq. (12). σ_{ITL} is expressed as a piecewise function due to piecewise l that is shown in Eq. (9):

- When $\alpha \leq \alpha_{critical}$, the interlayer tensile strength σ_{ITL} due to adhesive failure is represented by $\sigma'_{ITL,\,Adhesive}$ and calculated by Eq. (13), and that due to cohesive failure by $\sigma'_{ITL,\,Cohesive}$ and Eq. (14).

$$\sigma'_{ITL,Adhesive} = \sigma_{adhesion} \times \frac{(1-r)}{\cos\alpha \times (1 + 2\cos 2\alpha)} \tag{13}$$

$$\sigma'_{ITL,\,Cohesive} = \sigma_{cohesion} \times \frac{(1-r)}{3\cos\alpha} \tag{14}$$

These two failure modes are in a competitive relationship, meaning that the specimen fails if either one is initiated. Therefore, the adhesive failure is observed if $\sigma'_{\mathrm{ITL,\,Adhesive}} < \sigma'_{\mathrm{ITL,\,Cohesive}}$, cohesive failure if $\sigma'_{\mathrm{ITL,\,Adhesive}} > \sigma'_{\mathrm{ITL,\,Cohesive}}$, and mixed failure if $\sigma'_{\mathrm{ITL,\,Adhesive}} \approx \sigma'_{\mathrm{ITL,\,Cohesive}}$.

- When $\alpha > \alpha_{\mathrm{critical}}$, the interlayer tensile strength σ_{ITL} due to adhesive failure is represented by $\sigma''_{\mathrm{ITL,\,Adhesive}}$ and calculated by Eq. (15), and that due to cohesive failure by $\sigma''_{\mathrm{ITL,\,Cohesive}}$ and Eq. (16),

$$\sigma''_{\mathrm{ITL,\,Adhesive}} = \frac{\sigma_{\mathrm{adhesion}}}{1 + 2\cos 2\alpha} \tag{15}$$

$$\sigma''_{\mathrm{ITL,\,Cohesive}} = \frac{\sigma_{\mathrm{cohesion}}}{3} \tag{16}$$

Similar to the scenario when $\alpha \le \alpha_{\mathrm{critical}}$, the adhesive failure is observed if $\sigma''_{\mathrm{ITL,\,Adhesive}} < \sigma''_{\mathrm{ITL,\,Cohesive}}$, cohesive failure if $\sigma''_{\mathrm{ITL,\,Adhesive}} > \sigma''_{\mathrm{ITL,\,Cohesive}}$, and mixed failure if $\sigma''_{\mathrm{ITL,\,Adhesive}} \approx \sigma''_{\mathrm{ITL,\,Cohesive}}$. Furthermore, $\sigma''_{\mathrm{ITL,\,Cohesive}}$ equals to the matrix strength σ_{Matrix} conveniently since it corresponds to the cohesive failure when $\alpha > \alpha_{\mathrm{critical}}$ (e.g. $\alpha = 90^{\circ}$), which is satisfied by the tensile test setup for σ_{Matrix} in Section 2.4.

Transition angle $\alpha_{\mathrm{transition}}$ between the adhesive and cohesive failures is derived by $\sigma'_{\mathrm{ITL,\,Adhesive}} = \sigma'_{\mathrm{ITL,\,Cohesive}}$ or $\sigma''_{\mathrm{ITL,\,Adhesive}} = \sigma''_{\mathrm{ITL,\,Cohesive}}$, and expressed by,

$$\alpha_{\mathrm{transition}} = \frac{\cos^{-1}\left(\frac{3n-1}{2}\right)}{2} \tag{17}$$

where n is the strength ratio between interfacial adhesion and matrix cohesion, calculated by.

$$n = \frac{\sigma_{\mathrm{adhesion}}}{\sigma_{\mathrm{cohesion}}} (n \le 1) \tag{18}$$

Finally, interlayer strength σ_{ITL} is the minimum of $\sigma_{\mathrm{ITL,\,Adhesive}}$ and $\sigma_{\mathrm{ITL,\,Cohesive}}$, expressed by.

$$\sigma_{\mathrm{ITL}} = \begin{cases} \min\left(\sigma'_{\mathrm{ITL,\,Adhesive}},\ \sigma'_{\mathrm{ITL,\,Cohesive}}\right), \alpha \le \alpha_{\mathrm{critical}} \\ \min\left(\sigma''_{\mathrm{ITL,\,Adhesive}},\ \sigma''_{\mathrm{ITL,\,Cohesive}}\right), \alpha > \alpha_{\mathrm{critical}} \end{cases} \tag{19}$$

In this model, anisotropy is reflected only in the ultimate strength but not in elastic parameters following the insightful work by van den Heever *et al.* [32].

4.2. Validation of the theoretical model

In order to validate the theoretical model by the interlayer strength σ_{ITL} predicted in Eq. (19), interfacial adhesion $\sigma_{\mathrm{adhesion}} = 2.65\,(\mathrm{MPa})$ and matrix cohesion $\sigma_{\mathrm{cohesion}} = 7.06\,(\mathrm{MPa})$ are calculated for the present 3D printed concrete, by substitution of the interlayer strength with flat interface $\sigma_{\mathrm{ITL},\,0^{\circ}} = 0.36\,(\mathrm{MPa})$, matrix strength $\sigma_{\mathrm{Matrix}} = 2.35\,(\mathrm{MPa})$ and void ratio $r = 0.59$ into Eqs. (13) and (16). Interlayer strength σ_{ITL} subject to different tooth angles α between 0° and 90° is predicted by Eq. (19) with its four components $\sigma'_{\mathrm{ITL,\,Adhesive}}$, $\sigma'_{\mathrm{ITL,\,Cohesive}}$, $\sigma''_{\mathrm{ITL,\,Adhesive}}$ and $\sigma''_{\mathrm{ITL,\,Cohesive}}$, as shown in Fig. 20. The critical angle $\alpha_{\mathrm{critical}} = 66^{\circ}$ and transition angle $\alpha_{\mathrm{transition}} = 43^{\circ}$ are calculated by Eqs. (10) and (17).

Moreover, an envelope of σ_{ITL} is plotted with its upper and lower margins, showing an area where σ_{ITL} is observed with a higher probability. In order to compute the envelope margins, the upper limit of $\sigma_{\mathrm{ITL},\,0^{\circ}}$ is calculated by $(\sigma_{\mathrm{ITL},\,0^{\circ}})^{+} = \sigma_{\mathrm{ITL},\,0^{\circ}} + \mathrm{Std}(\sigma_{\mathrm{ITL},\,0^{\circ}}) = 0.59(\mathrm{MPa})$, and the lower limit of $\sigma_{\mathrm{ITL},\,0^{\circ}}$ is calculated by $(\sigma_{\mathrm{ITL},\,0^{\circ}})^{-} = \sigma_{\mathrm{ITL},\,0^{\circ}} - \mathrm{Std}(\sigma_{\mathrm{ITL},\,0^{\circ}}) = 0.14(\mathrm{MPa})$. Similarly, the limits of $\sigma_{\mathrm{ITL},\,90^{\circ}}$ (a.k.a. the matrix strength σ_{Matrix}) and the limits of void ratio r are calculated by the mean plus or minus the standard deviation, namely $(\sigma_{\mathrm{ITL},\,90^{\circ}})^{+} = 3.10\,(\mathrm{MPa})$, $(\sigma_{\mathrm{ITL},\,90^{\circ}})^{-} = 1.61\,(\mathrm{MPa})$, $(r)^{+} = 0.72$, and $(r)^{-} = 0.46$. The upper margin of the σ_{ITL} envelope is then computed by substitution of $(\sigma_{\mathrm{ITL},\,0^{\circ}})^{+}$, $(\sigma_{\mathrm{Matrix}})^{+}$ and $(r)^{-}$ into Eqs. (13), (16) and then (19), while the lower margin is computed with $(\sigma_{\mathrm{ITL},\,0^{\circ}})^{-}$, $(\sigma_{\mathrm{Matrix}})^{-}$ and $(r)^{+}$. It is found that the experimental interlayer strengths $\sigma_{\mathrm{ITL},\,15^{\circ}}$ and $\sigma_{\mathrm{ITL},\,45^{\circ}}$ with tooth angles $\alpha = 15^{\circ}$ and $\alpha = 45^{\circ}$ are very close to those predicted by the theoretical model with relative errors of 6.6 % and 4.0 %, and the experimental data are fully included between the upper and lower margins of the σ_{ITL} envelope. Furthermore, the mixed mode of adhesive and cohesive failures in the tensile test with tooth angle $\alpha = 45^{\circ}$ is also explained by the tooth angle α close to the transition angle $\alpha_{\mathrm{transition}} = 43^{\circ}$.

Although this model is developed for the interlayer tensile strength σ_{ITL}, interlayer shear strength τ_{ITL} in the direction I is also predictable with the same technique. Interfacial adhesion $\tau_{\mathrm{adhesion}} = 16.27\,(\mathrm{MPa})$ and matrix cohesion $\tau_{\mathrm{cohesion}} = 22.23\,(\mathrm{MPa})$ in terms of shear are computed by Eqs. (13) and (16), and then the interlayer shear strength τ_{ITL} is plotted together with its four components $\tau'_{\mathrm{ITL,\,Adhesive}}$, $\tau'_{\mathrm{ITL,\,Cohesive}}$, $\tau''_{\mathrm{ITL,\,Adhesive}}$ and $\tau''_{\mathrm{ITL,\,Cohesive}}$, as

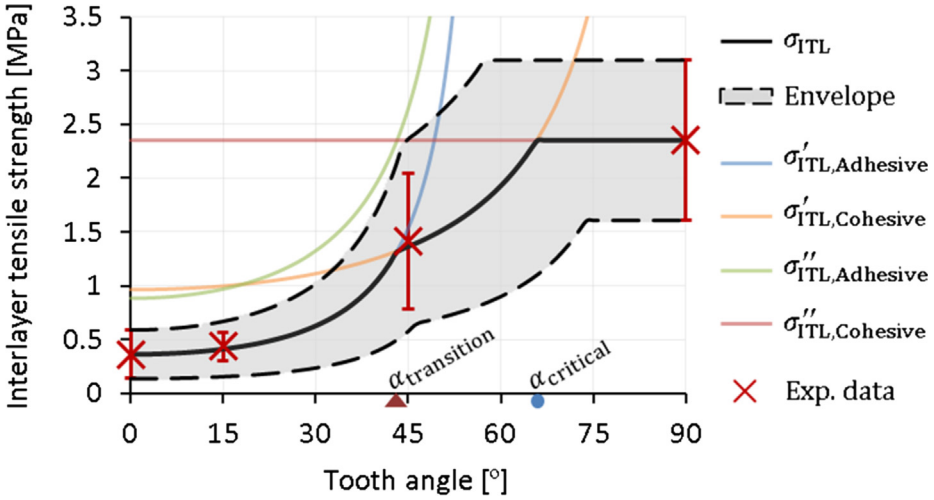

Fig. 20. Comparison between the predicted and measured interlayer tensile strengths.

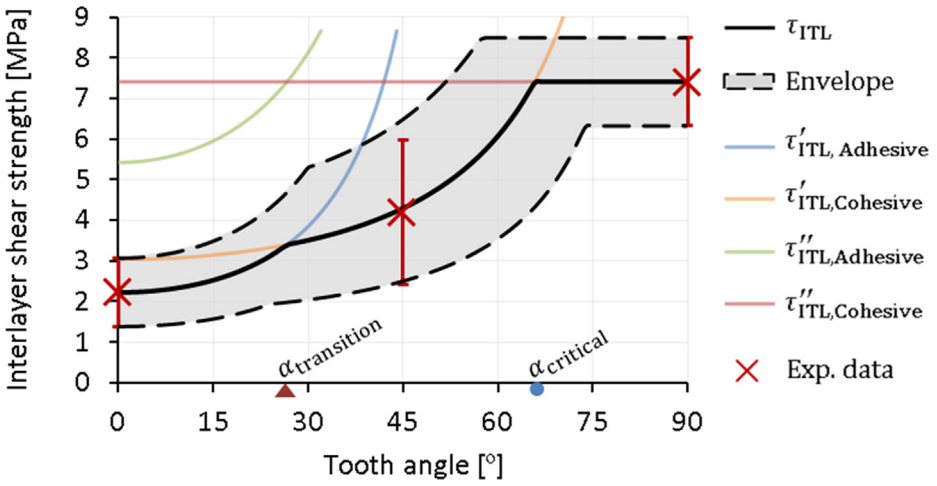

Fig. 21. Comparison between the predicted and measured interlayer shear strengths.

shown in Fig. 21. The τ_{ITL} envelope in grey colour with the upper and lower margins illustrates the area where τ_{ITL} is observed with a higher probability. It is found that the experimental data $\tau_{ITL\ I,\ 45^\circ}$ also falls close to the predicted strength with its error bar almost entirely included in the envelope.

4.3. Generalization of the theoretical model

In order to generalize this model, non-dimensional strengths $R'_{Adhesive}$, $R'_{Cohesive}$, $R''_{Adhesive}$ and $R''_{Cohesive}$ of the 3D printed concrete are calculated respectively by dividing $\sigma'_{ITL,\ Adhesive}$, $\sigma'_{ITL,\ Cohesive}$, $\sigma''_{ITL,\ Adhesive}$ and $\sigma''_{ITL,\ Cohesive}$ with the matrix strength σ_{Matrix}, such that.

- if $\alpha \le \alpha_{critical}$,

$$R'_{Adhesive} = \frac{3 \times n \times (1-r)}{(1+2\cos 2\alpha) \times \cos\alpha} \tag{20}$$

$$R'_{Cohesive} = \frac{(1-r)}{\cos\alpha} \tag{21}$$

- if $\alpha > \alpha_{critical}$,

$$R''_{Adhesive} = \frac{3 \times n}{(1+2\cos 2\alpha)} \tag{22}$$

$$R''_{Cohesive} = 1 \tag{23}$$

It is observed from Eqs. (20)–(23) that the non-dimensional strengths are composed by four elements: n is related to the interfacial adhesion and matrix cohesion, $(1-r)$ related to the content of interfacial voids, $3(1+2\cos 2\alpha)^{-1}$ related to the tooth angle α due to the stress concentration phenomenon, and $(\cos\alpha)^{-1}$ related to α due to the variation of interfacial area. The $(\cos\alpha)^{-1}$ element is also interpreted as the interaction between two neighbour voids, such that the stress concentration areas locate side by side with strong interaction if $\alpha = 0$, while the stress concentration areas are deviated if $\alpha > 0$ and thus the interaction is weakened. It is also noticed that $(\cos\alpha)^{-1}$ vanishes when $\alpha > \alpha_{critical}$, and if the void ratio $r \approx 0$, $\alpha_{critical} = \cos^{-1}(1-r) \approx 0$. Therefore, $(\cos\alpha)^{-1}$ does not make contribution if $r \approx 0$ since the interaction is already negligible between faraway voids. In order to study the influences of

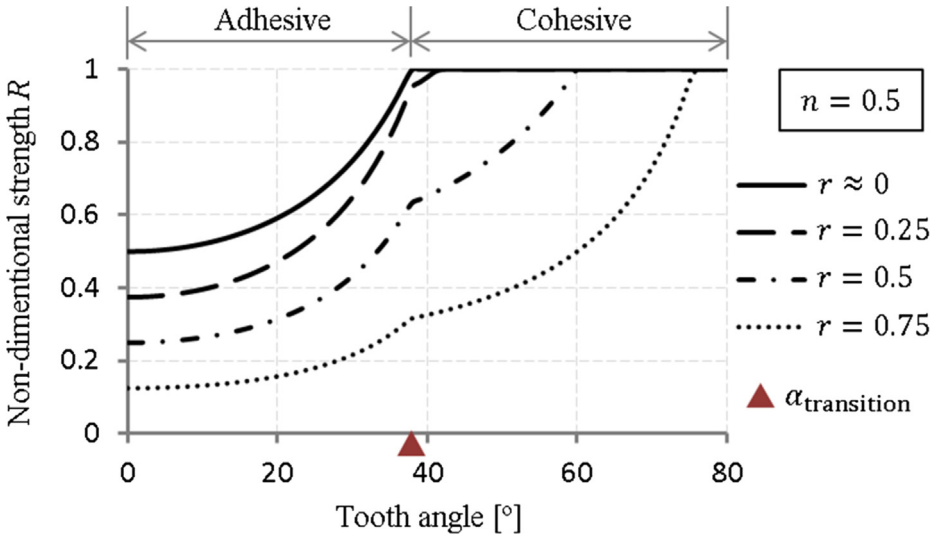

Fig. 22. Non-dimensional interlayer strength R against the interfacial tooth angle α subject to strength ratio $n = 0.5$ and different void ratios r.

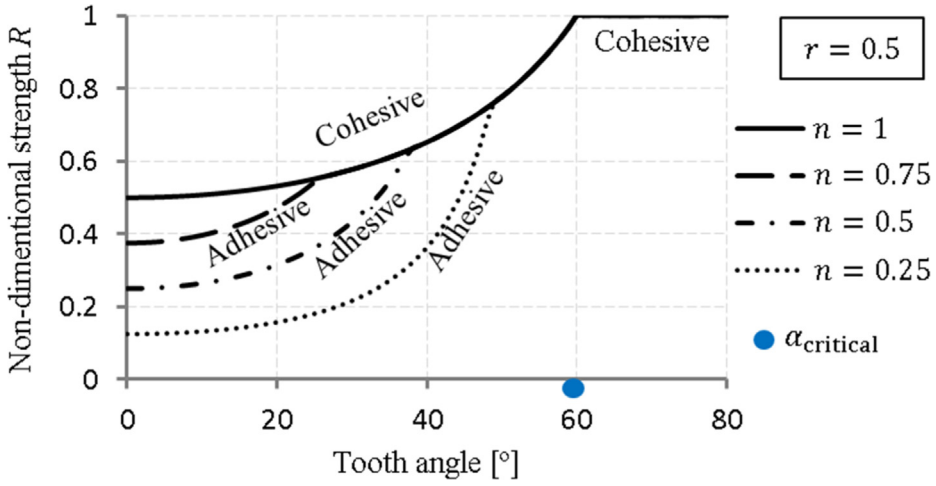

Fig. 23. Non-dimensional interlayer strength R against the interfacial tooth angle α subject to void ratio $r = 0.5$ and different strength ratios n.

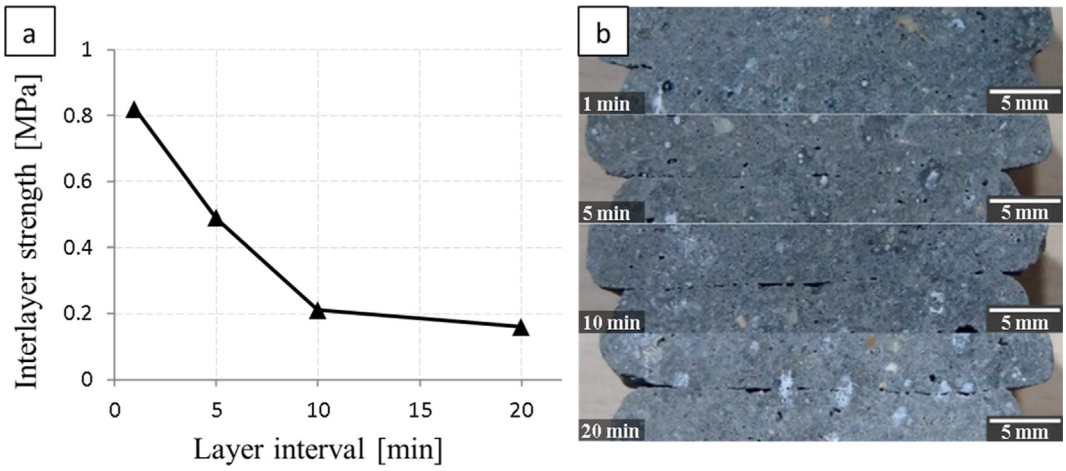

Fig. 24. (a) Interlayer tensile strengths and (b) interfacial voids subject to different layer intervals by Ref. [12]. Figure redrawn from the journal Virtual and Physical Prototyping, 14 (2019) 104–113, Y.W.D. Tay, G.H.A. Ting, Y. Qian, B. Panda, L. He, M.J. Tan, Time gap effect on bond strength of 3D-printed concrete [12], with permission from Taylor & Francis ltd, www.tandfonline.com.

strength ratio n, void ratio r and tooth angle α on the non-dimensional interlayer strength R, Eqs. (20)–(23) are finally combined into,

$$R = \begin{cases} \min\left(R'_{\text{Adhesive}}, R'_{\text{Cohesive}}\right), \alpha \le \alpha_{\text{critical}} \\ \min\left(R''_{\text{Adhesive}}, R''_{\text{Cohesive}}\right), \alpha > \alpha_{\text{critical}} \end{cases} \tag{24}$$

As shown in Figs. 22-23, R is plotted against the tooth angle α subject to different interfacial void ratios r and strength ratios n. It is observed that higher void ratio r and lower strength ratio n result in lower non-dimensional interlayer strength R for the specimens with flat interface ($\alpha = 0^{\circ}$). However, this degradation of strength is compensated by a proper interfacial tooth angle α, such that larger α is required for higher void ratio r and lower strength ratio n. It is also seen that the increase of non-dimensional strength R against the tooth angle α is nonlinear, such that the increase is very slow with small α, while it becomes much faster when α is larger. Therefore, a careful design of the tooth angle α is required based on the actual demand of the interlayer strength. Furthermore, the interlayer failure shifts from adhesive mode to cohesive one at the transition angle $\alpha_{\text{transition}}$ which is fully determined by the strength ratio n, and thus interlayer strength with smaller tooth angle α is more affected by interfacial adhesion σ_{adhesion}, whereas that with larger α is more affected by matrix cohesion σ_{cohesion}. Meanwhile, the critical angle α_{critical} depends only on the void ratio r since α_{critical} represents the smallest tooth angle with negligible interaction between two neighbour voids. Last but not least, homogeneity is achieved in the printed concrete with the

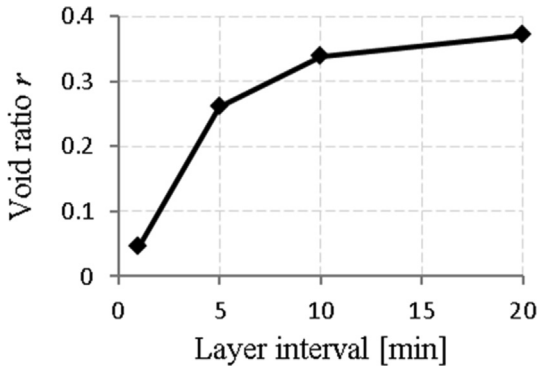

Fig. 25. Interfacial void ratios r subject to different layer intervals.

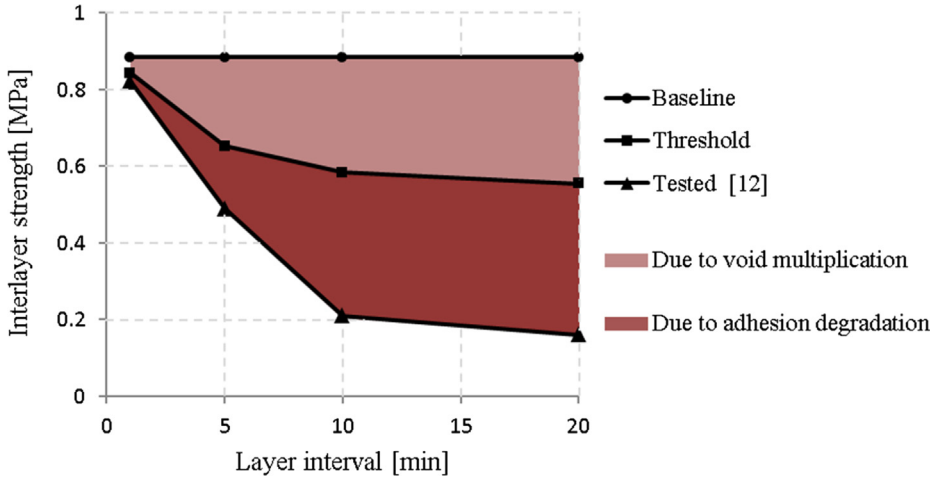

Fig. 26. Impacts of void multiplication and adhesion degradation on the interlayer strength subject to different layer intervals.

interlayer strength σ_{ITL} equal to the matrix strength σ_{Matrix}, if the tooth angle α is larger than both the transition angle $\alpha_{transition}$ and critical angle $\alpha_{critical}$.

4.4. Case study and discussions

In the theoretical model, degradation of the interfacial adhesion $\sigma_{adhesion}$ and increase of the interfacial void ratio r are the two direct causes of the decrease of the interlayer strength. It is assumed that the degradation of interfacial adhesion $\sigma_{adhesion}$ is related to hydration, since a portion of active ingredients in the previous layer is already consumed by hydration if the layer interval is too long, and thus the chemical reactions between the layers is weakened [24]. Meanwhile, the increase of interfacial void ratio r is related to the development of stiffness and static yield stress [12,66], probably due to thixotropy [24,67], moisture evaporation [14], or hydration [68]. Therefore, when the previous layer becomes stiff, more air voids are entrapped at the interface during the deposition of fresh concrete [12].

In order to distinguish and quantify the impacts of the two causes, a case study is conducted. As shown in Fig. 24, Ref. [12] measured the interlayer tensile strengths and photographed the interfaces with different layer intervals. Based on these pictures, the interfacial void ratios r are measured and plotted, as shown in Fig. 25. A strength baseline $T_{baseline}$ indicating the interlayer strength before the decrease is then plotted, as shown in Fig. 26, by substitution of the void ratio $r \approx 0$, tooth angle $\alpha = 0^{\circ}$ and interfacial adhesion $\sigma_{adhesion} = 2.65(\text{MPa})$ into Eq. (13) ($\sigma_{adhesion}$ calculated by the present study also applies to Ref. [12] since the same material is adopted). A strength threshold $T_{threshold}$ reflecting the strength due to only the impact of the interfacial voids is calculated by substitution of the just measured void ratios r into the same Eq. (13). Therefore, the impact of adhesion degradation is the gap between the threshold and the tested strength, since tooth angle $\alpha = 0^{\circ}$ is constant due to the flat interface and the remaining two factors on the interlayer strength are the interfacial void ratio r and interfacial adhesion $\sigma_{adhesion}$.

Impact coefficients I of the void multiplication and adhesion degradation are calculated respectively by,

$$I_{void} = (T_{baseline} - T_{threshold})/T_{baseline} \tag{25}$$

$$I_{adhesion} = (T_{threshold} - T_{tested})/T_{threshold} \tag{26}$$

The corresponding contribution ratios are then calculated by,

$$\Psi_{void} = I_{void}/(I_{void} + I_{adhesion}) \tag{27}$$

$$\Psi_{adhesion} = I_{adhesion}/(I_{void} + I_{adhesion}) \tag{28}$$

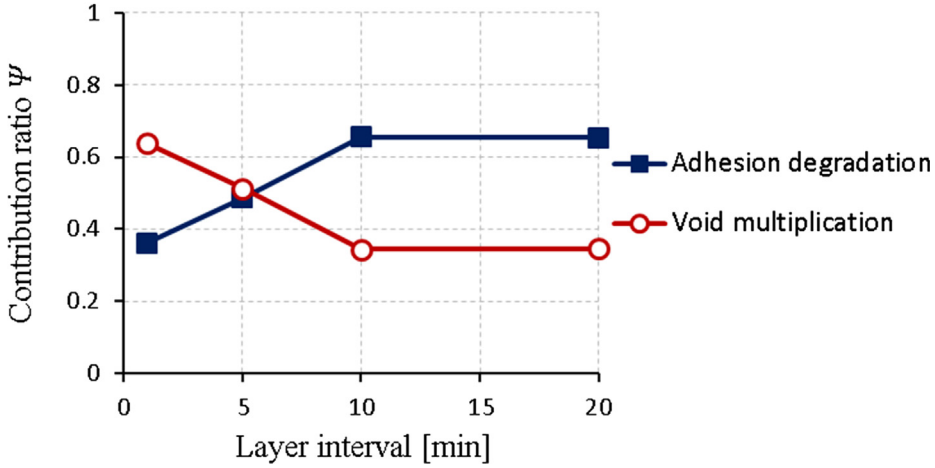

Fig. 27. Contribution ratios Ψ of the adhesion degradation and void multiplication subject to different layer intervals.

As shown in Fig. 27, the contribution ratio of void multiplication Ψ_{void} starts at about 64 % and then decreases to about 51 % at 5 mins and 34 % at 10 mins, indicating that thixotropy and moisture evaporation play major roles when the concrete is just deposited, but then their effects weaken in the following 10 mins. It is also seen that the contribution ratios Ψ_{void} and $\Psi_{adhesion}$ become synchronized and stable after 10 mins, implying that in this case the development of mechanical properties (e.g. stiffness and static yield stress) are mainly contributed by the hydration.

Moreover, this result also suggests that emphasis should be placed on the reduction of interfacial voids with short layer interval, such as to maintain the moisture [6], reduce the nozzle standoff distance [5], and adopt vibration-assisted printing [25,69,70]. If the layer interval becomes longer, the contribution of adhesion degradation becomes more important and thus focus should be placed more on the enhancement of interfacial adhesion. A balance between retarder and accelerator might be found, in order to retard the hydration in the previous layer [8,71,72] but not to affect the hydration rate in the other layers.

However, the above-mentioned techniques have their limitations. The superficial moisture of the printed layers will lose quickly if the printing is conducted in some harsh environment, and the layer interval will be extremely long if a large-scale structure is printed or the pipe is clogged during the printing. In these circumstances, tooth-like interface is recommended for increasing the interlayer strength and producing monolithic concrete structures. The effect of the tooth-like interface increases with the tooth angle α, until the maximum interlayer strength is achieved when α is larger than both the transition angle α_T and critical angle α_C. Therefore, careful calculation of the optimum tooth angle α is essential, based on the void ratio r and strength ratio n subject to different printing materials and conditions.

5. Conclusions

Tooth-like layer interfaces with different tooth angles are generated by 3D concrete printing, and then the interlayer tensile and shear strengths are measured for the specimens with reserved or removed interlayer notch. It is found that the specimens with removed interlayer notch reveal the effect of interfacial tooth angle better, such that the interlayer strength increases with the tooth angle with a nonlinear rate in both the tensile and shear tests. Moreover, interfacial tooth angle of 45° generates a mixed mode of adhesive and cohesive failures, while tooth angle of 15° or the flat interface produces only pure adhesive failure.

A theoretical model of the interlayer strength is also proposed based on the different mechanisms of adhesive and cohesive failures, for a type of low-slump concrete 3D printed by cavity pump with a printing speed of 80 mm/s and layer interval of about 10 s. In this model, the interlayer strength is expressed analytically by interface parameters including the tooth angle, the void ratio, and the ratio between interfacial adhesion and matrix cohesion. It is shown that larger tooth angle shifts the interlayer failure mode from adhesive failure to cohesive one, and increases the interlayer strength until the interlayer strength is equal to the matrix strength. Validation of this model is also performed, with the relative error of about 5 % between the predicted and the measured interlayer strengths.

Through a case study, the impacts of interfacial void and adhesion degradation on the interlayer strength are calculated and compared based on the proposed theoretical model. It is found that the impact of interfacial void is more significant when the layer interval is shorter than 5 mins, while adhesion degradation becomes more influential with longer layer interval. Therefore, it is necessary to compute the interfacial void ratio and adhesion degradation on a case by case basis, and then adopt the optimal interfacial tooth angle predicted by the theoretical model for a higher interlayer strength of 3D printed concrete.

Data availability

Data will be made available on request.

Declaration of Competing Interest

The authors declare that they have no known competing financial interests or personal relationships that could have appeared to influence the work reported in this paper.

Acknowledgements

The authors acknowledge the financial and technical supports from National Research Foundation of Singapore, SempCorp Design & Construction Pte Ltd., and Singapore Centre for 3D Printing (SC3DP). This work is also supported by Young-scientist Research Cultivation Program of South China Normal University under Grant 21KJ15, in part by the Guangdong Basic and Applied Basic Research Project under Grant 2021A1515011171, and in part by the National Natural Science Foundation of China under Grant 62076103.

References

[1] Y.W.D. Tay, B. Panda, S.C. Paul, N.A. Noor Mohamed, M.J. Tan, K.F. Leong, 3D printing trends in building and construction industry: a review, Virtual Phys. Prototyp. 12 (3) (2017) 261–276, https://doi.org/10.1080/17452759.2017.1326724.
[2] G. Ma, L. Wang, Y. Ju, State-of-the-art of 3D printing technology of cementitious material—an emerging technique for construction, Sci. China Technol. Sci. 61 (4) (2018) 475–495, https://doi.org/10.1007/s11431-016-9077-7.
[3] T. Wangler, N. Roussel, F.P. Bos, T.A.M. Salet, R.J. Flatt, Digital concrete: a review, Cem. Concr. Res. 123 (2019) 105780, https://doi.org/10.1016/j.cemconres.2019.105780.
[4] B. Zareiyan, B. Khoshnevis, Interlayer adhesion and strength of structures in Contour Crafting - Effects of aggregate size, extrusion rate, and layer thickness, Autom. Constr. 81 (2017) 112–121, https://doi.org/10.1016/j.autcon.2017.06.013.
[5] B. Panda, S.C. Paul, N.A.N. Mohamed, Y.W.D. Tay, M.J. Tan, Measurement of tensile bond strength of 3D printed geopolymer mortar, Measurement 113 (2018) 108–116, https://doi.org/10.1016/j.measurement.2017.08.051.
[6] J.G. Sanjayan, B. Nematollahi, M. Xia, T. Marchment, Effect of surface moisture on inter-layer strength of 3D printed concrete, Constr. Build. Mater. 172 (2018) 468–475, https://doi.org/10.1016/j.conbuildmat.2018.03.232.
[7] A.J. Babafemi, J.T. Kolawole, M.J. Miah, S.C. Paul, B. Panda, A concise review on interlayer bond strength in 3D concrete printing, Sustainability 13 (13) (2021) 7137, https://doi.org/10.3390/su13137137.
[8] H. Ye, X. Gao, L. Zhang, Influence of time-dependent rheological properties on distinct-layer casting of self-compacting concrete, Constr. Build. Mater. 199 (2019) 214–224, https://doi.org/10.1016/j.conbuildmat.2018.12.025.
[9] B. Panda, S.C. Paul, L.J. Hui, Y.W.D. Tay, M.J. Tan, Additive manufacturing of geopolymer for sustainable built environment, J. Cleaner Prod. 167 (2017) 281–288, https://doi.org/10.1016/j.jclepro.2017.08.165.
[10] S.C. Paul, Y.W.D. Tay, B. Panda, M.J. Tan, Fresh and hardened properties of 3D printable cementitious materials for building and construction, Arch. Civ. Mech. Eng. 18 (1) (2018) 311–319, https://doi.org/10.1016/j.acme.2017.02.008.
[11] B. Panda, S. Chandra Paul, M. Jen Tan, Anisotropic mechanical performance of 3D printed fiber reinforced sustainable construction material, Mater. Lett. 209 (2017) 146–149, https://doi.org/10.1016/j.matlet.2017.07.123.
[12] Y.W.D. Tay, G.H.A. Ting, Y.e. Qian, B. Panda, L. He, M.J. Tan, Time gap effect on bond strength of 3D-printed concrete, Virtual Phys. Prototyp. 14 (1) (2019) 104–113, https://doi.org/10.1080/17452759.2018.1500420.
[13] B. Panda, S. Ruan, C. Unluer, M.J. Tan, Improving the 3D printability of high volume fly ash mixtures via the use of nano attapulgite clay, Compos. Part B-Eng. 165 (2019) 75–83, https://doi.org/10.1016/j.compositesb.2018.11.109.
[14] R.J.M. Wolfs, F.P. Bos, T.A.M. Salet, Hardened properties of 3D printed concrete: the influence of process parameters on interlayer adhesion, Cem. Concr. Res. 119 (2019) 132–140, https://doi.org/10.1016/j.cemconres.2019.02.017.
[15] H. Xie, G. Li, G. Xiong, Microstructure model of the interfacial zone between fresh and old concrete, J. Wuhan Univ. Technol.-Mater Sci. Ed. 17 (2002) 64–68, https://doi.org/10.1007/BF02838421.

[16] A.D. Espeche, J. León, Estimation of bond strength envelopes for old-to-new concrete interfaces based on a cylinder splitting test, Constr. Build. Mater. 25 (3) (2011) 1222–1235, https://doi.org/10.1016/j.conbuildmat.2010.09.032.
[17] H. Beushausen, B. Höhlig, M. Talotti, The influence of substrate moisture preparation on bond strength of concrete overlays and the microstructure of the OTZ, Cem. Concr. Res. 92 (2017) 84–91, https://doi.org/10.1016/j.cemconres.2016.11.017.
[18] Y. He, X. Zhang, R.D. Hooton, X. Zhang, Effects of interface roughness and interface adhesion on new-to-old concrete bonding, Constr. Build. Mater. 151 (2017) 582–590, https://doi.org/10.1016/j.conbuildmat.2017.05.049.
[19] H. Beushausen, M.G. Alexander, Bond strength development between concretes of different ages, Mag. Concr. Res. 60 (1) (2008) 65–74, https://doi.org/10.1680/macr.2007.00108.
[20] B. Zareiyan, B. Khoshnevis, Effects of interlocking on interlayer adhesion and strength of structures in 3D printing of concrete, Autom. Constr. 83 (2017) 212–221, https://doi.org/10.1016/j.autcon.2017.08.019.
[21] L. Courard, T. Piotrowski, A. Garbacz, Near-to-surface properties affecting bond strength in concrete repair, Cem. Concr. Compos. 46 (2014) 73–80, https://doi.org/10.1016/j.cemconcomp.2013.11.005.
[22] V.N. Nerella, S. Hempel, V. Mechtcherine, Effects of layer-interface properties on mechanical performance of concrete elements produced by extrusion-based 3D-printing, Constr. Build. Mater. 205 (2019) 586–601, https://doi.org/10.1016/j.conbuildmat.2019.01.235.
[23] B. Panda, N.A. Noor Mohamed, S.C. Paul, G. Bhagath Singh, M.J. Tan, B. Savija, The effect of material fresh properties and process parameters on buildability and interlayer adhesion of 3D printed concrete, Materials 12 (2019) 31277393, https://doi.org/10.3390/ma12132149.
[24] N. Roussel, Rheological requirements for printable concretes, Cem. Concr. Res. 112 (2018) 76–85, https://doi.org/10.1016/j.cemconres.2018.04.005.
[25] J.G. Sanjayan, R. Jayathilakage, P. Rajeev, Vibration induced active rheology control for 3D concrete printing, Cem. Concr. Res. 140 (2021) 106293, https://doi.org/10.1016/j.cemconres.2020.106293.
[26] T. Marchment, J. Sanjayan, M. Xia, Method of enhancing interlayer bond strength in construction scale 3D printing with mortar by effective bond area amplification, Mater. Design 169 (2019) 107684, https://doi.org/10.1016/j.matdes.2019.107684.
[27] J. Kruger, G. van Zijl, A compendious review on lack-of-fusion in digital concrete fabrication, Addit. Manuf. 37 (2021) 101654, https://doi.org/10.1016/j.addma.2020.101654.
[28] E. Secrieru, D. Cotardo, V. Mechtcherine, L. Lohaus, C. Schröfl, C. Begemann, Changes in concrete properties during pumping and formation of lubricating material under pressure, Cem. Concr. Res. 108 (2018) 129–139, https://doi.org/10.1016/j.cemconres.2018.03.018.
[29] E. Secrieru, J. Khodor, C. Schröfl, V. Mechtcherine, Formation of lubricating layer and flow type during pumping of cement-based materials, Constr. Build. Mater. 178 (2018) 507–517, https://doi.org/10.1016/j.conbuildmat.2018.05.118.
[30] M. van den Heever, A. du Plessis, J. Kruger, G. van Zijl, Evaluating the effects of porosity on the mechanical properties of extrusion-based 3D printed concrete, Cem. Concr. Res. 153 (2022) 106695, https://doi.org/10.1016/j.cemconres.2021.106695.
[31] J. Kruger, A. du Plessis, G. van Zijl, An investigation into the porosity of extrusion-based 3D printed concrete, Addit. Manuf. 37 (2021) 101740, https://doi.org/10.1016/j.addma.2020.101740.
[32] M. van den Heever, F. Bester, J. Kruger, G. van Zijl, Mechanical characterisation for numerical simulation of extrusion-based 3D concrete printing, J. Build. Eng. 44 (2021) 102944, https://doi.org/10.1016/j.jobe.2021.102944.
[33] M. van den Heever, A. du Plessis, F. Bester, J. Kruger, G. van Zijl, A mechanistic evaluation relating microstructural morphology to a modified Mohr-Griffith compression-shear constitutive model for 3D printed concrete, Constr. Build. Mater. 325 (2022) 126743, https://doi.org/10.1016/j.conbuildmat.2022.126743.
[34] B.A. Tayeh, B.H. Abu Bakar, M.A. Megat Johari, Y.L. Voo, Mechanical and permeability properties of the interface between normal concrete substrate and ultra high performance fiber concrete overlay, Constr. Build. Mater. 36 (2012) 538–548, https://doi.org/10.1016/j.conbuildmat.2012.06.013.
[35] D.K. Harris, J. Sarkar, T.M. Ahlborn, Characterization of interface bond of ultra-high-performance concrete bridge deck overlays, Transp. Res. Record: J. Transp. Res. Board 2240 (1) (2011) 40–49, https://doi.org/10.3141/2240-07.
[36] M.E. Mohamad, I.S. Ibrahim, R. Abdullah, A.B. Abd, A.B.H. Rahman, J.U. Kueh, Friction and cohesion coefficients of composite concrete-to-concrete bond, Cem. Concr. Compos. 56 (2015) 1–14, https://doi.org/10.1016/j.cemconcomp.2014.10.003.
[37] Y.e. Qian, D. Zhang, T. Ueda, Interfacial tensile bond between substrate concrete and repairing mortar under freeze-thaw cycles, J. Adv. Concr. Technol. 14 (8) (2016) 421–432, https://doi.org/10.3151/jact.14.421.
[38] R. Mirmoghtadaei, M. Mohammadi, N. Ashraf Samani, S. Mousavi, The impact of surface preparation on the bond strength of repaired concrete by metakaolin containing concrete, Constr. Build. Mater. 80 (2015) 76–83, https://doi.org/10.1016/j.conbuildmat.2015.01.018.
[39] L.i. Wang, Y.i. Liu, Y.u. Yang, Y. Li, M. Bai, Bonding performance of 3D printing concrete with self-locking interfaces exposed to compression–shear and compression–splitting stresses, Addit. Manuf. 42 (2021) 101992, https://doi.org/10.1016/j.addma.2021.101992.
[40] L. He, W.T. Chow, H. Li, Effects of interlayer notch and shear stress on interlayer strength of 3D printed cement paste, Addit. Manuf. 36 (2020) 101390, https://doi.org/10.1016/j.addma.2020.101390.
[41] L. He, J.Z.M. Tan, W.T. Chow, H. Li, J. Pan, Design of novel nozzles for higher interlayer strength of 3D printed cement paste, Addit. Manuf. 48 (2021) 102452, https://doi.org/10.1016/j.addma.2021.102452.
[42] E. Hosseini, M. Zakertabrizi, A.H. Korayem, G. Xu, A novel method to enhance the interlayer bonding of 3D printing concrete: an experimental and computational investigation, Cem. Concr. Compos. 99 (2019) 112–119, https://doi.org/10.1016/j.cemconcomp.2019.03.008.
[43] Y. Weng, M. Li, T.N. Wong, M.J. Tan, Synchronized concrete and bonding agent deposition system for interlayer bond strength enhancement in 3D concrete printing, Autom. Constr. 123 (2021) 103546, https://doi.org/10.1016/j.autcon.2020.103546.
[44] Y. Ding, A.M. Abdullah, M. Dunn, K. Yu, Design of interfaces to promote the bonding strength between dissimilar materials, J. Manuf. Processes 76 (2022) 786–795, https://doi.org/10.1016/j.jmapro.2022.02.060.
[45] Y. Weng, M. Li, D. Zhang, M.J. Tan, S. Qian, Investigation of interlayer adhesion of 3D printable cementitious material from the aspect of printing process, Cem. Concr. Res. 143 (2021) 106386, https://doi.org/10.1016/j.cemconres.2021.106386.
[46] J. Xiao, H. Liu, T. Ding, Finite element analysis on the anisotropic behavior of 3D printed concrete under compression and flexure, Addit. Manuf. 39 (2021) 101712, https://doi.org/10.1016/j.addma.2020.101712.
[47] R.A. Buswell, W.R. Leal de Silva, S.Z. Jones, J. Dirrenberger, 3D printing using concrete extrusion: a roadmap for research, Cem. Concr. Res. 112 (2018) 37–49, https://doi.org/10.1016/j.cemconres.2018.05.006.
[48] R.J.M. Wolfs, F.P. Bos, T.A.M. Salet, Early age mechanical behaviour of 3D printed concrete: numerical modelling and experimental testing, Cem. Concr. Res. 106 (2018) 103–116, https://doi.org/10.1016/j.cemconres.2018.02.001.
[49] D. Asprone, F. Auricchio, C. Menna, V. Mercuri, 3D printing of reinforced concrete elements: technology and design approach, Constr. Build. Mater. 165 (2018) 218–231, https://doi.org/10.1016/j.conbuildmat.2018.01.018.
[50] J.H. Lim, B. Panda, Q.-C. Pham, Improving flexural characteristics of 3D printed geopolymer composites with in-process steel cable reinforcement, Constr. Build. Mater. 178 (2018) 32–41, https://doi.org/10.1016/j.conbuildmat.2018.05.010.
[51] H. Ogura, V. Nerella, V. Mechtcherine, Developing and testing of strain-hardening cement-based composites (SHCC) in the context of 3D-printing, Materials 11 (2018) 1375, https://doi.org/10.3390/ma11081375.
[52] M.P. Savruk, A. Kazberuk, Stress concentration near sharp and rounded V-notches in orthotropic and quasi-orthotropic bodies, ThAFM 84 (2016) 166–176, https://doi.org/10.1016/j.tafmec.2016.02.006.
[53] L. Náhlík, K. Štegnerová, P. Hutař, Estimation of critical applied stress for crack initiation from a sharp V-notch, ThAFM 93 (2018) 247–262, https://doi.org/10.1016/j.tafmec.2017.09.002.
[54] A. Carpinteri, P. Cornetti, N. Pugno, A. Sapora, On the most dangerous V-notch, IJSS 47 (7-8) (2010) 887–893, https://doi.org/10.1016/j.ijsolstr.2009.11.017.
[55] H. Baghi, J.A.O. Barros, Shear properties of the strain hardening cementitious composite material, J. Mater. Civ. Eng. 28 (2016) 04016093, https://doi.org/10.1061/(asce)mt.1943-5533.0001603.
[56] V.C. Li, D.K. Mishra, A.E. Naaman, J.K. Wight, J.M. LaFave, H.-C. Wu, Y. Inada, On the shear behavior of engineered cementitious composites, Adv. Cem. Based Mater. 1 (3) (1994) 142–149, https://doi.org/10.1016/1065-7355(94)90045-0.
[57] M. Chilwesa, F. Minelli, A. Reggia, G. Plizzari, Evaluating the shear bond strength between old and new concrete through a new test method, Mag. Concr. Res. 69 (9) (2017) 425–435, https://doi.org/10.1680/jmacr.16.00327.
[58] J. Zhang, X. Ding, Q. Zhao, Experimental and numerical investigation of scattering gravels on the surface bond strength of self-compacting concrete, Constr. Build. Mater. 145 (2017) 11–19, https://doi.org/10.1016/j.conbuildmat.2017.03.219.
[59] D.S. Santos, P.M.D. Santos, D. Dias-da-Costa, Effect of surface preparation and bonding agent on the concrete-to-concrete interface strength, Constr. Build. Mater. 37 (2012) 102–110, https://doi.org/10.1016/j.conbuildmat.2012.07.028.
[60] S. Austin, P. Robins, Y. Pan, Shear bond testing of concrete repairs, Cem. Concr. Res. 29 (7) (1999) 1067–1076, https://doi.org/10.1016/S0008-8846(99)00088-5.
[61] G.P.A.G. van Zijl, Improved mechanical performance: Shear behaviour of strain-hardening cement-based composites (SHCC), Cem. Concr. Res. 37 (8) (2007) 1241–1247, https://doi.org/10.1016/j.cemconres.2007.04.009.
[62] G.N. Savin, Stress distribution around holes, National Aeronautics and Space Administration (1970).
[63] X. Xu, L. Sun, X. Fan, Stress concentration of finite composite laminates with elliptical hole, Computers Struct. 57 (1) (1995) 29–34, https://doi.org/10.1016/0045-7949(94)00588-T.
[64] M.H. Sadd, Elasticity: theory, applications, and numerics, Second ed., (2009), https://doi.org/10.1016/B978-0-12-374446-3.X0001-6.
[65] W.D. Pilkey, D.F. Pilkey, Peterson's Stress Concentration Factors, Third Edition (2008), https://doi.org/10.1002/9780470211106.
[66] N. Roussel, F. Cussigh, Distinct-layer casting of SCC: The mechanical consequences of thixotropy, Cem. Concr. Res. 38 (5) (2008) 624–632, https://doi.org/10.1016/j.cemconres.2007.09.023.
[67] Y. Qian, S. Kawashima, Use of creep recovery protocol to measure static yield stress and structural rebuilding of fresh cement pastes, Cem. Concr. Res. 90 (2016) 73–79, https://doi.org/10.1016/j.cemconres.2016.09.005.
[68] B. Panda, J.H. Lim, M.J. Tan, Mechanical properties and deformation behaviour of early age concrete in the context of digital construction, Compos. Part B-Eng. 165 (2019) 563–571, https://doi.org/10.1016/j.compositesb.2019.02.040.

[69] T.J. Fleck, J.C.S. McCaw, S.F. Son, I.E. Gunduz, J.F. Rhoads, Characterizing the vibration-assisted printing of high viscosity clay material, Addit. Manuf. 47 (2021) 102256, https://doi.org/10.1016/j.addma.2021.102256.
[70] J.A. Koch, D.I. Castaneda, R.H. Ewoldt, D.A. Lange, Vibration of fresh concrete understood through the paradigm of granular physics, Cem. Concr. Res. 115 (2019) 31–42, https://doi.org/10.1016/j.cemconres.2018.09.005.
[71] A. Baskoca, M.H. Ozkul, S. Artirma, Effect of chemical admixtures on workability and strength properties of prolonged agitated concrete, Cem. Concr. Res. 28 (5) (1998) 737–747, https://doi.org/10.1016/S0008-8846(98)00029-5.
[72] X. Chen, Y. Guo, B. Li, M. Zhou, B. Li, Z. Liu, J. Zhou, Coupled effects of the content and methylene blue value (MBV) of microfines on the performance of manufactured sand concrete, Constr. Build. Mater. 240 (2020), https://doi.org/10.1016/j.conbuildmat.2019.117953 117953.